INSTITUTE OF PHYSICS PUBLISHING JOURNAL OF PHYSICS B: ATOMIC, MOLECULAR AND OPTICAL PHYSICS

J. Phys. B: At. Mol. Opt. Phys. **39** (2006) R79–R125 doi:10.1088/0953-4075/39/5/R01

TOPICAL REVIEW

Open shells and multi-electron interactions: core level photoionization of the 3d metal atoms

Michael Martins[1], Kai Godehusen[2], Tobias Richter[3], Philippe Wernet[2] and Peter Zimmermann[3]

[1] Institut für Experimentalphysik, Universität Hamburg, Luruper Chaussee 149, D-22761 Hamburg, Germany
[2] BESSY GmbH, Albert-Einstein-Str. 15, D-12489 Berlin, Germany
[3] Institut für Atomare Physik und Fachdidaktik, Technische Universität Berlin, Hardenbergstr. 36, D-10623 Berlin, Germany

E-mail: michael.martins@desy.de

Received 28 October 2005, in final form 2 December 2005
Published 6 February 2006
Online at stacks.iop.org/JPhysB/39/R79

Abstract

This review covers the outer core level photoionization of the free 3d metal atoms from Sc to Cu. The experimental 3p, 3s and 2p photoemission and photoabsorption spectra are discussed. A comparison emphasizes common features and distinct differences. The interpretation of the data based on *ab initio* calculations reveals the influence of multi-electron interactions in the 3d metal atoms. We focus on the fundamental effects and main interactions which govern the electronic structure of these open shell atoms.

(Some figures in this article are in colour only in the electronic version)

1. Introduction

This review reports on the core level photoionization of free 3d transition metal atoms from Sc to Cu. Understanding the complex electronic structure of these open shell elements with all the involved multi-electron interactions is important for many fields in physics and technology.

The 3d valence electrons are responsible for the outstanding magnetic and electronic properties of the 3d transition metals and compounds. Core level photoionization is an ideal tool to gain element specific information on properties induced by the 3d electrons. Unique information can be obtained by exciting the 2p or 3p electrons into the unoccupied 3d valence orbitals or into the continuum. Due to the core hole influence on the valence electrons, gas phase experiments are well suited to study core–valence interactions.

The magnetism of the 3d transition metals and in particular the magnetic properties of thin films are crucial for modern data storage technology. The ferromagnetic late transition metals Fe, Co and Ni are of particular relevance. An important discovery was the giant magnetic resistance (GMR) [1–4], which was first observed by Grünberg *et al* [1] in Fe/Cr multilayers.

The GMR is explained by the magnetic coupling in ultra thin films of ferromagnetic and antiferromagnetic materials like Cr or Mn. The discovery of the GMR was the key point in the development of modern reading heads for high density storage in today's common computer hard disks.

Complex compounds of type $La_{1-x}Ca_xMnO_3$ have also attracted much interest, due to the observation of a phenomenon which is referred to as colossal magnetoresistance (CMR) [5, 6]. It turns out that a wealth of intra- and inter-atomic correlation effects like charge, spin and orbital ordering is responsible for the properties of these manganite materials [7–10]. The origin of orbital ordering is the exchange interaction between neighbouring 3d transition metal ions, which strongly depends on the spatial orientation of occupied d orbitals [11, 12]. As has been reported by Castleton and Altarelli [9] and Elfimov *et al* [8], it should be possible to make a direct observation of orbital ordering in many manganite and similar materials using core level spectroscopy at the L-edges or at the K-edge; see also recent experimental results of Mannella *et al* [13].

The theoretical analysis of core level spectra of transition metals and compounds is often based on atomic models. Simple one-electron models can describe the magnetic dichroism of metals [14–16] whereas more complicated semi-empirical models based on atomic multiplet theory are needed to analyse the core level spectra of compounds [17–19]. The analysis of the spectra is often hampered by peak broadening due to solid state effects or highly correlated ground states due to charge transfer effects. The atomic data can be very useful as a reference to disentangle intra- and inter-atomic effects.

This review presents experimental 3p and 2p photoabsorption and direct 3p, 3s and 2p photoemission spectra of free 3d metal atoms together with detailed theoretical analysis. Further and more complicated effects in the resonant core level photoemission (e.g., [20–29]), in the angular distribution of photoelectrons [30], the dichroism effects in free 3d metal atoms [31–36], or the photoionization of 3d metal compounds [37, 38] are not discussed in detail here.

2. Theoretical aspects

The general Hamiltonian of a many-electron atom can be written as

$$\begin{aligned}\mathcal{H} &= \sum_i \mathcal{H}_{\mathrm{kin,i}} + \mathcal{H}_{\mathrm{Nucl,i}} + \mathcal{H}_{\mathrm{SO,i}} + \sum_{k\neq i} \mathcal{H}_{\mathrm{Coul,ik}} \\ &= \sum_i \frac{\hbar^2}{2m}\nabla_i^2 - \frac{1}{4\pi\epsilon_0}\frac{Ze^2}{r_i} + \zeta_i(r_i)(\vec{\ell}_i \cdot \vec{s}_i) + \sum_{k\neq i}\frac{1}{4\pi\epsilon_0}\frac{e^2}{r_i - r_k}. \end{aligned} \tag{1}$$

∇_i^2 is the operator of the kinetic energy and r_i is the coordinate of the electron i. Ze^2/r_i describes the Coulomb interaction of the electron i with the nucleus. The last term $\sum_{k\neq i} e^2/(r_i - r_k)$ is the interaction of the electron i with all other electrons in the atom. In equation (1) only the spin–orbit operator $\mathcal{H}_{\mathrm{SO,i}}$ as the most important relativistic contribution is included. $\mathcal{H}_{\mathrm{SO,i}}$ is a single-electron operator and describes only the spin–orbit interaction of the electron i by the spin–orbit parameter $\zeta_i(r_i)$. Relativistic two-particle interactions of different electrons i and k (spin–spin, orbit–orbit, spin–other-orbit) are usually much smaller. Further relativistic effects can be taken into account by including the mass and the Darwin operator $\mathcal{H}_M$ and $\mathcal{H}_D$, respectively [39].

What is the main problem in solving the corresponding Schrödinger or, for a fully relativistic manner treatment, the Dirac equation? The solutions for the first two terms $(\mathcal{H}_{\mathrm{kin,i}} + \mathcal{H}_{\mathrm{Nucl,i}})$ are simply hydrogenic wavefunctions, as the coordinates of individual

electrons are separated. The problem lies in the term $(r_i - r_k)^{-1}$, which describes the Coulomb interaction of electrons. With this Coulomb interaction or correlation term the Schrödinger equation is no longer analytically solvable.

Using highly sophisticated theoretical methods (see, e.g., [40] and references therein) the electronic structure and the photoionization of the simplest many-body problem in atomic physics, the helium atom or helium like ions, can be described almost perfectly [41, 42]. Further atoms studied very intensely in the gas phase are the other rare gases (Ne, Ar, Kr, Xe), due to their closed shell structure [43, 44]. This closed shell structure allows theoretical studies using advanced methods like the random phase approximation (RPA) [45] or the many-body perturbation theory (MBPT) [46, 47]. The problem in the case of the transition metals is their open shell character. Strong correlations between a large number of states have to be taken into account for an accurate description.

The basic approximation for many-electron atoms is the mean-field approximation based on the independent-particle model. In this approximation, it is assumed that every particle is moving in the mean field generated by all other particles. This concept is used in the well-known Hartree–Fock (HF) self-consistent field (SCF) method for the calculation of the wavefunctions in the independent-particle model. In the HF method the correlation term $(r_i - r_k)^{-1}$ is approximated by an effective, mean potential $V_{i,\mathrm{HF}}$ created by the $k \neq i$ electrons. Relativistic effects are taken into account as perturbations. In cases like for heavy atoms, where fully relativistic calculations are necessary, the Dirac–Fock (DF) method has to be applied.

The most important relativistic term is the spin–orbit operator $\mathcal{H}_{\mathrm{SO}}$ which is not included in the (standard) Hartree–Fock (HF) method. The spin–orbit interaction is calculated by applying the Blume–Watson method [48, 49], which also includes the spin–other-orbit operator $\mathcal{H}_{\mathrm{SOO},ik}$. This method is often referred to as relativistic Hartree–Fock (RHF).

Throughout this review, the term HF is used for the restricted HF method. In the restricted HF method the spin dependence of the radial wavefunction is neglected, and all electrons of a subshell $n\ell$ are described by the same radial wavefunction $\psi_{n\ell}$. In the unrestricted HF method different radial wavefunctions are used for spin-up and spin-down electrons.

In terms of the Slater–Condon theory [50, 51] an atomic wavefunction Ψ^k is described as an expansion into known basis functions ψ_b of a single-electron configuration

$$\Psi^k = \sum_b y_b^k \psi_b \tag{2}$$

where ψ_b is given by the Slater determinant of one-electron wavefunctions φ_k to fulfil the Pauli principle.

2.1. Correlation effects

The HF includes multiplet-splitting effects, as described by the Slater integrals F^k (direct part) and G^k (exchange part) [50, 39]:

$$\begin{aligned} F^k(n_i\ell_i n_j\ell_j) &= \frac{e^2}{4\pi\epsilon_0}\int\!\!\int \frac{r_<^k}{r_>^{k+1}} P_{n_i\ell_i}(r_1)^2 P_{n_j\ell_j}(r_2)^2 \,\mathrm{d}r_1\,\mathrm{d}r_2 \\ G^k(n_i\ell_i n_j\ell_j) &= \frac{e^2}{4\pi\epsilon_0}\int\!\!\int \frac{r_<^k}{r_>^{k+1}} P_{n_i\ell_i}(r_1)^* P_{n_i\ell_i}(r_2) P_{n_j\ell_j}(r_1)^* P_{n_j\ell_j}(r_2) \,\mathrm{d}r_1\,\mathrm{d}r_2. \end{aligned} \tag{3}$$

$P_{n\ell}(r)$ is the radial part of the one-electron wavefunction.

Sometimes already this multiplet splitting is referred to as a correlation effect. In this review, however, the term electron correlation will be used for effects which are not included

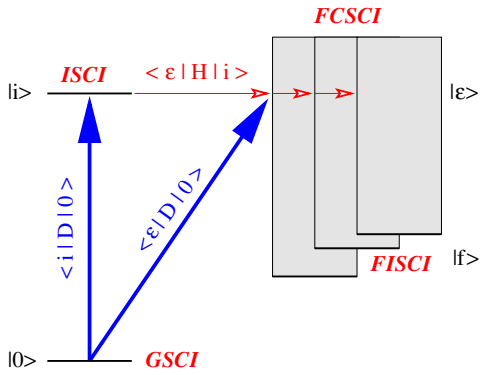

Figure 1. Correlations in different states of an atom. $\langle i|\mathcal{D}|0\rangle$ and $\langle\epsilon|\mathcal{D}|0\rangle$ are the dipole matrix elements between the ground state $|0\rangle$ and the intermediate and continuum states, respectively. $V_\epsilon = \langle\epsilon|\mathcal{H}|i\rangle$ is the Coulomb matrix element between the intermediate state $|i\rangle$ and the continuum $|\epsilon\rangle$.

in the mean-field approximation. Correlations are described here in terms of configuration interaction (CI). CI is introduced by the generalized Slater integrals R^k:

$$R^k(n_i\ell_i n_j\ell_j, n_p\ell_p n_q\ell_q) = \frac{e^2}{4\pi\epsilon_0}\iint \frac{2r_<^k}{r_>^{k+1}} P_{n_i\ell_i}(r_1)^* P_{n_j\ell_j}(r_2)^* P_{n_p\ell_p}(r_1) P_{n_q\ell_q}(r_2)\,\mathrm{d}r_1\,\mathrm{d}r_2. \tag{4}$$

For any excitation or de-excitation process correlations can be taken into account for the ground state, the final state and also for possible intermediate states. In figure 1 this is sketched for the different states involved in a photoionization process. In this case, we distinguish between correlations in the ground state $|0\rangle$ (ground state configuration interaction, GSCI) and in a discrete intermediate state $|i\rangle$ (intermediate state configuration interaction, ISCI). The notation used here is the same as in [52]. Sometimes, for example, by Schmidt [44], ISCI is used for initial state configuration interaction, which is named GSCI here. Furthermore, in the photoionization process correlations between the continuum states $|\epsilon\rangle$ (final continuum state configuration interaction, FCSCI) and the final ionic state $|f\rangle$ (final ionic state configuration interaction, FISCI) can occur. Depending on the atom, correlations in the various states will have different contributions. For example, in the case of atomic barium, the main correlation effect on the direct 4d and 5p photoelectron emission is due to FISCI, whereas GSCI is only of minor importance [53–55]. In FISCI the continuum electron is not included in the interaction. The continuum electron acts therefore only as a spectator. In FCSCI the continuum electron is directly involved in the interaction. FCSCI is one model to describe, for example, interchannel coupling. Interchannel coupling has significant effects on the angular distribution of photoelectrons, for example, in the region of the xenon 4d shape resonance [56] or above threshold [57].

For the exact calculation of correlation effects, an infinite number of configurations of the same parity has to be included. However, in practice this is not feasible and one has to limit to a reasonable number of configurations. Configurations with the largest expected CI mixing coefficients are selected. In table 1 the typical CI expansion for Mn is listed. But, in general, calculations taking into account only this so-called strong CI with a limited configuration set do not give the correct energy spread of the multiplet. As has been shown by Rajnak and Wybourne [58, 59] this can be understood as a result of the cumulative effect of CI with the infinite number of high-lying configurations. These configurations will have only very small

Table 1. Definition of correlations in different states of an atom. In the last column as an example a simple configuration interaction (CI) expansion is shown for Mn with the ground state $|0\rangle = 3d^5 4s^2\ {}^6S_{5/2}$.

GSCI	Ground state CI	$3d^5 4s^2 + 3d^6 4s + 3d^7$
ISCI	Intermediate state CI	$3p^5 3d^6 4s^2 + 3p^5 3d^7 4s + 3p^5 3d^8$
FISCI	Final ionic state CI	$3d^4 4s^2 + 3d^5 4s + 3d^6$
FCSCI	Final continuum state CI	$3d^4 4s^2 \epsilon\ell + 3d^3 4s^2 4d\epsilon'\ell$

mixing coefficients, their influence is therefore often referred to as weak CI. They will squeeze upper configuration terms more than the lower ones, thereby contributing to a compression of the width of the configuration. Weak CI is included by scaling the Coulomb Slater integrals [50]. For neutral atoms typical values are 80–85% of their *ab initio* values ([39], chapter 16-2). The approach that is expected to be most accurate is the explicit inclusion of strong CI together with the implicit inclusion of weak CI via scaling factors.

The CI calculations which have been performed for the 3d metal atoms are based on the so-called Slater–Condon superposition-of-configuration method. In this method, the wavefunctions and therefore the Slater integrals of all configurations are optimized using the (R)HF approximation for every configuration separately.

Several configurations can be optimized simultaneously in the SCF process, which is done in the multi-configuration HF (MCHF) or the corresponding fully relativistic multi-configuration DF (MCDF) method. They are superior to the CI method, because the correlations are included already in the SCF process. However, this is more complex and it is much more complicated to reach convergence, in particular for excited states. Note that Hibbert in [60] and others use the term 'CI' for MCHF calculations.

2.2. The photoionization process

The photoionization process can be described as the ionization of an atom A by a photon $h\nu$ resulting in an ionized atom A^+ and a photoelectron e^-:

$$A + h\nu \rightarrow A^+ + e^-. \tag{5}$$

To describe this process completely, the ground state of the atom A, the final state of the ion A^+, the state of the emitted electron e^-, and the state of the photon $h\nu$ have to be known.

In electron spectroscopy three fundamental processes can be distinguished within the independent-particle model (figure 2). Direct photoemission (a) leads to a singly ionized atom. A created core hole will decay via an Auger process (b). The probability for radiative decay of 3p or 2p core holes for the 3d transition metals is much smaller than the Auger probability (less than 1%) [61]. The resonant process (c) can be described in a first-order approximation as a two-step process with a resonant excitation into an intermediate state and a subsequent independent Auger decay. This picture is valid only if the Auger process is relatively slow. For very fast processes or for a narrow band excitation this separation into two steps is no longer valid and the whole excitation/decay has to be handled as a one-step process.

The processes and the corresponding matrix elements involved in the photoionization are sketched in figure 1. A ground state $|0\rangle$ is excited by photons to an intermediate, resonant state $|i\rangle$ or directly into a continuum state $|\epsilon\rangle$. Note that what is called the ground state in the experiment, is not necessarily the ground state of the atom. Some therefore favour the term 'initial state'. $\langle i|\mathcal{D}|0\rangle$ and $\langle\epsilon|\mathcal{D}|0\rangle$ are the dipole matrix elements between the ground state and

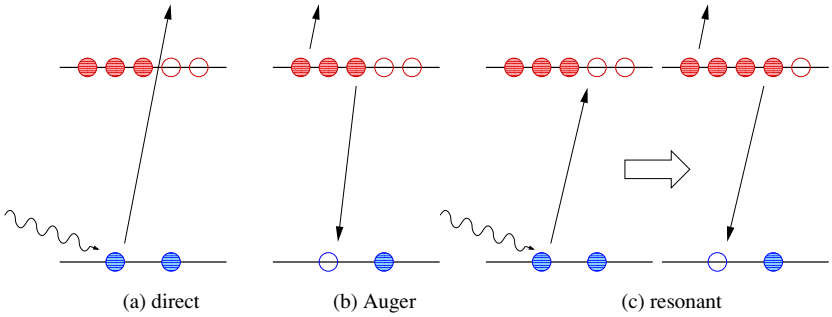

Figure 2. Schematic illustration of the fundamental electron-emission processes in the independent-particle model. (a) Direct photoemission. (b) Decay of a core hole by Auger electron emission. (c) Resonant photoemission illustrated here as a resonant excitation followed by an Auger decay. Possible satellite processes, such as shake up, shake down or shake off processes, are not shown.

the intermediate and continuum state, respectively. In the XUV region with photon energies $h\nu$ from 10 eV up to a few 100 eV the wavelength λ of the radiation is on the order of 1–100 nm which justifies the use of the dipole approximation. The intermediate state $|i\rangle$ may decay into the continuum state $|\epsilon\rangle$ through the Auger matrix element $\langle\epsilon|\mathcal{H}|i\rangle$. This matrix element has the form of a generalized Slater integral $R^k(n_i\ell_i n_j\ell_j, n_p\ell_p\epsilon\ell)$ between two states with different configurations, where the second state represents the photoion with the outgoing photoelectron $\epsilon\ell$. Auger transition rates strongly depend on the overlap of the corresponding radial wavefunctions $P_{n\ell}$. For $n_1 = n_2 = n_3$ the spatial overlap is maximal giving rise to very fast Auger transitions (super–Coster–Kronig, SCK). This results, for example, in the large line width of the 3p absorption spectra (see section 4.1), which is about one order of magnitude larger than for the 2p absorption spectra, even though there are more possible decay channels in the latter case.

2.3. Photoionization resonances

One method to describe the interaction of an intermediate state $|i\rangle$ with a continuum state $|\epsilon\rangle$ is the famous theory proposed by Fano [62]. In the Fano theory the final state $|\Psi^k\rangle = |f\rangle$ is described as a linear combination of the discrete (intermediate) states $|\psi^k\rangle = |i^k\rangle$ and the continuum states $|\varphi_\epsilon\rangle = |\epsilon\rangle$; the index k numbers different resonances.

For the case of a single discrete state and one continuum, the final state $|f^k\rangle$ can be described by

$$\left|f_\epsilon^k\right\rangle = a_\epsilon^k \cdot |i^k\rangle + \int b_{\epsilon,\epsilon'}^k \cdot |\epsilon'\rangle \, \mathrm{d}\epsilon'. \tag{6}$$

This ansatz leads to the well-known Fano formula

$$\sigma(\eta) \propto \frac{(q+\eta)^2}{1+\eta^2} \tag{7}$$

for the resonance profile. The Fano parameter q and the normalized resonance position η are given by

$$q = \frac{d_{\mathrm{dis}}}{\pi d_{\mathrm{cont}} V_\epsilon} \tag{8}$$

$$\eta = \frac{h\nu - E}{\pi |V_\epsilon|^2}, \tag{9}$$

with the photon energy $h\nu$ and the resonance position E. $d_{\mathrm{dis}} = \langle i|\mathcal{D}|0\rangle$, $d_{\mathrm{cont}} = \langle \epsilon|\mathcal{D}|0\rangle$, and $V_\epsilon = \langle \epsilon|\mathcal{H}_{\mathrm{Coul}}|i\rangle$ are the dipole matrix elements between the ground state and the intermediate state, the ground state and the continuum state, and the Coulomb matrix element between the intermediate state and the continuum, respectively. V_ϵ has the form of a CI matrix element. This theory is, for example, derived in the textbook of Cowan [39]. The Fano theory is valid in the case of overlapping resonances for one discrete state and one continuum state, one discrete state and several continuum states and several discrete states and one continuum state. It can also be used for several discrete states and several continua in the case of non-overlapping resonances.

To describe overlapping resonances in the case of more than one continuum state, the Fano theory was extended by Mies [63]. A similar method was published later by Davis and Feldkamp [64, 65]. Using the formalism of Mies, the total cross section is given as a sum over the partial cross sections

$$\sigma_{\mathrm{tot}} = \sum_j \sigma_j = \sum_j |D_j|^2. \tag{10}$$

The dipole matrix elements

$$D_j = \langle f^j|\mathcal{D}|0\rangle \tag{11}$$

between the ground state $|0\rangle$ and the final states of the photoionization process $|f^j\rangle$ are given as the components of the vector

$$\mathbf{D} = (1 + \mathrm{i}\mathbf{K})^{-1}(\mathbf{d}_{\mathrm{cont}} + \mathbf{V}^*(h\nu - \mathbf{E})^{-1}\mathbf{d}_{\mathrm{dis}}) \tag{12}$$

with

$$\mathbf{K} = \mathbf{V}^*(h\nu - \mathbf{E})^{-1}\mathbf{V}. \tag{13}$$

Here $\mathbf{V} = (V_{jk}) = (\langle \epsilon_j|\mathcal{H}_{\mathrm{Coul}}|i_k\rangle)$ is the Coulomb matrix between the intermediate states $|i_k\rangle$ and the continuum states $|\epsilon_j\rangle$. $\mathbf{d}_{\mathrm{cont}} = (d_{\mathrm{cont},j}) = (\langle \epsilon_j|\mathcal{D}|0\rangle)$ and $\mathbf{d}_{\mathrm{dis}} = (d_{\mathrm{dis},k}) = (\langle i_k|\mathcal{D}|0\rangle)$ are the dipole matrix elements between the ground state $|0\rangle$, the continuum states and the intermediate states, respectively. j and k are the indices of the different continuum and intermediate states, respectively.

For overlapping resonances the extended Fano theory should be used to describe the photoionization process. This is particularly the case for the 3p $\rightarrow$ 3d absorption of the 3d metals, which will be discussed in section 4.1.

2.4. Numerical methods

Sophisticated methods, taking into account the many-body character of the problem, such as the many-body perturbation theory (MBPT), the random phase approximation (RPA) or multi-configuration methods (e.g., MCHF) accurately describe correlation effects. In principle, these methods can be used to describe the atomic structure and photoionization processes of all atoms. However, in practice, they are mostly limited to closed shell atoms, because for open shell atoms the number of terms, which have to be included is too large. There are attempts, for example, by Altun and Manson, to adapt the MBPT to open shell atoms [47, 66–68].

An alternative method to calculate the photoionization process of open shell atoms has been developed in the past decade. This method has been successfully used to describe the core level photoionization of a large number of 3d, 5d and 4f transition metal atoms [69–74]. It is based on CI calculations for the atomic structure using the Cowan code [39] and the extended Fano formalism for the photoionization process [75].

Another quite successful method to calculate the photoionization process is the R-matrix theory [76]. In R-matrix calculations, the configuration space is divided into an inner and

an outer region. In the inner region, the photoionized or scattered electron is treated as indistinguishable from the other $(N-1)$ electrons of the atom or ion and the full N-electron problem is solved. In the outer region, the photoelectron interacts with the target as a whole and is described by asymptotic functions. The $(N-1)$-electron target is characterized by a multipole potential and the R-matrix condition connects the wavefunction of both regions at the boundary. R-matrix calculations are used in the stellar opacity project [77, 78] or the IRON project [79] to calculate cross-section data for the analysis of plasma and astrophysical data. Most of these calculations were limited to the outer shells and the valence region, like for Fe and Ni by Nahar *et al* [80] and Bautista [81, 82]. First calculations in the core level region of the 3d elements have been presented: Donnelly *et al* [83–86] calculated the 3p–3d excitation for Cr, Mn and their ions. Berrington [87, 88] performed the first R-matrix calculations for the 3p–3d excitation of Fe and some Fe ions. For highly ionized Fe XV calculations have been performed by Bautista up to the K-shell [89]. Some results have also been obtained by Gorczyca *et al* for the Sc^{3+} recombination cross section [90]. Photoemission calculations for the 3d transition metals using the R-matrix method have not been presented yet.

For complex atoms like the 3d transition metals and their ions, the R-matrix method will need a large amount of CPU time, on the order of several thousand CPU hours on a supercomputer [91]. The R-matrix theory includes, in particular, also the excitation into Rydberg states for the included channels up to infinity. However, for most of the 2p and 3p core level photoabsorption spectra, Rydberg excitations are only of minor importance. The extended Fano method will need less CPU time and is a well-suited method to calculate the core level photoionization process of the 3d metal atoms.

3. Experimental techniques

Early results on the photoabsorption of 3d metal atoms were obtained with the aid of an arc source with a monochromator and with photographic plates to record the spectra; see, e.g., the review article of Sonntag and Zimmermann [92]. However, these experiments were mostly limited by the flux of the photon sources. Nowadays, synchrotron radiation (SR) is used for most photoionization experiments with free 3d metal atoms. In the following sections, the fundamentals of synchrotron radiation and metal vapour sources and the basic principles of photoionization experiments are presented.

3.1. Synchrotron radiation

In table 2 the photon energies needed for core level ionization of solid 3d transition metals are listed. The energies vary between 30 and 80 eV for 3p and several keV for 1s ionization. These edges can all be accessed with synchrotron radiation sources which offer highly brilliant radiation from the infrared up to the hard x-ray region with tunable photon energies. Synchrotron radiation based techniques are hence the methods of choice to investigate 3d metal photoionization.

Synchrotron radiation was first observed by Elder *et al* [94, 95] and theoretically described by Schwinger [96]. Particle accelerators, designed for high energy physics, are nowadays considered to be the so-called first generation of synchrotron radiation sources. These sources were not built and optimized for the generation of synchrotron radiation. Nevertheless, they allowed completely new experiments, like the first observation of doubly excited states in free helium atoms by Madden and Codling [97].

The second generation of synchrotron radiation sources such as BESSY I (Berliner Elektronen Speicherring-Gesellschaft für Synchrotronstrahlung m.b.H., Berlin, Germany) or

Table 2. Solid state core electron binding energies of 3d transition metals taken from [93].

	Binding energy (eV) Electron subshell				
	3p	3s	2p	2s	1s
Sc	28	51	399–404	498	4492
Ti	33	59	454–460	561	4966
V	37	66	512–520	627	5465
Cr	42	74	574–584	696	5989
Mn	47	82	639–650	769	6539
Fe	53	91	707–720	845	7112
Co	59	101	778–793	925	7709
Ni	66–68	111	852–870	1009	8333
Cu	75–77	122	932–952	1097	8979

the SRC (Synchrotron Radiation Center, Wisconsin, USA) were the first machines dedicated to the generation and application of synchrotron radiation. These machines were optimized for the generation of synchrotron radiation with bending magnets.

With the advent of third-generation synchrotron radiation facilities such as the Advanced Light Source (ALS, Berkeley, USA) or BESSY II in Berlin, enormous progress was achieved. The main difference of the third-generation sources compared to the older sources is the extensive use of so-called insertion devices such as wigglers and, in particular, undulators, which are inserted into the straight sections of the storage rings to produce highly collimated radiation. Both systems are periodic arrangements of magnetic structures. In a wiggler, the emitted radiation is an incoherent superposition of the synchrotron radiation from all individual magnet structures, resulting in an enhanced intensity by a factor N, where N is the number of magnetic periods. In addition to the higher intensity, the spectrum of a wiggler is identical to that of a normal bending magnet used in second-generation sources. In undulators, the superposition of the radiation from individual magnetic structures is coherent. This enhances the brilliance and hence the flux available at the experiment by a factor N^2. However, the spectrum is not continuous, but consists of several comparably sharp peaks, with, in the first order, a width $E/\Delta E = N$. For a detailed description, see, e.g., the review of Wille [98].

3.2. High temperature metal atom beam sources

For the generation of 3d metal atom beams high temperature ovens are often employed. Sufficient target density in the interaction region typically requires a vapour pressure on the order of 10^{-2} hPa inside the crucible of the oven. The temperatures needed for this vapour pressure are listed in table 3. To achieve the high temperatures, crucibles made of molybdenum or tantalum are often used and heated either resistively or by electron impact [99]. Typical heating powers are in the order of 80–300 W. Several of the 3d metals are liquid at the required temperatures (see the melting points in table 3) and form highly reactive melts. To avoid reactions of these aggressive metal melts with the crucible material insets made of Al_2O_3 or graphite can be used. High density beams are comparably easy to produce for Cr and Mn because these metals sublime at the required temperatures.

The high temperatures in the vapour may lead to a population of excited initial states due to the Boltzmann distribution. This population can be described by

$$w_i = (2J_i + 1) \cdot \exp\left(-\frac{E_i - E_0}{k_B T}\right). \tag{14}$$

Table 3. Evaporation temperatures corresponding to 10^{-2} hPa vapour pressure and melting points for the 3d elements. Contributions of different initial states as caused by the thermal population in an atomic beam evaporated at the temperature given in the second column. Only for V and Ni are two different electronic configurations populated; see the text for details.

	Evaporation temperature (K)	Melting point (K)	Initial states			Contribution
Sc	1663	1814	$4s^2$	3d	$^2D_{3/2,5/2}$	44%, 56%
Ti	2003	1941	$4s^2$	$3d^2$	$^3F_{2,3,4}$	28%, 34%, 38%
V	2123	2163	$4s^2$	$3d^3$	$^4F_{3/2,5/2,7/2,9/2}$	14%, 19%, 22%, 24%
			4s	$3d^4$	$^6D_{1/2,3/2,5/2,7/2,9/2}$	2%, 3%, 5%, 6%, 7%
Cr	1668	2133	4s	$3d^5$	$^7S_3$	100%
Mn	1243	1518	$4s^2$	$3d^5$	$^6S_{5/2}$	100%
Fe	1743	1808	$4s^2$	$3d^6$	$^5D_{4,3,2,1,0}$	48%, 27%, 15%, 8%, 2%
Co	1813	1768	$4s^2$	$3d^7$	$^4F_{9/2,7/2,5/2,3/2}$	58%, 24%, 12%, 6%
Ni	1803	1726	$4s^2$	$3d^8$	$^3F_{4,3,2}$	41%, 11%, 4%
			4s	$3d^9$	$^3D_{3,2,1}$	27%, 11%, 4%
Cu	1533	1355	4s	$3d^{10}$	$^2S_{1/2}$	100%

where E_0 is the ground state energy, and E_i and J_i are the energy and the angular momentum of state i, respectively.

Table 3 shows that in all 3d metal atoms except for Cr, Mn and Cu several initial states are populated at the given evaporation temperature. For V and Ni the thermal excitation even leads to a population of two different electron configurations. Note that the ground states of the 3d metal atoms are well described in LS-coupling.

3.3. Photoabsorption spectroscopy

The Lambert Beer law $I = I_0 \cdot \exp(-\sigma \cdot n \cdot l)$ relates the photon energy dependent absorption cross section $\sigma(h\nu)$, the density n of the atoms or molecules and the absorption length l with the initial photon flux I_0 and the measured photon flux I after absorption by the sample. One way to measure the photoabsorption cross section is thus to measure the intensity I transmitted through the sample. Most of the older work on photoabsorption of metal vapours relies on this method and is summarized in the review of Sonntag and Zimmermann [92]. This approach is also used, for example, in the dual laser plasma (DLP) [100] method, where the emission of a laser-produced plasma is used as a vacuum-ultraviolet (VUV) source and a second laser is used to evaporate the absorbing material [101–103]. The spectra are recorded using a high-resolution Rowland circle monochromator and a position-sensitive detector. The detector is both rotated and translated to always fulfil the Rowland circle condition. This method is very useful for studying materials with very high evaporation temperatures such as tungsten [104] and free ions, because ions are abundant in the absorbing plasma generated by the second laser. However, the high plasma temperatures in the order of several eV (several 10 000 K) are often disadvantageous, due to the large number of states which can be populated at these temperatures [105, 106].

The detection of ions is another way to measure the photoabsorption cross section. Here, ions created in the decay process subsequent to the core level excitation are detected. This can be done either in a simple gas cell, by counting all ions by measuring the photocurrent (total ion yield) or by counting single ions with a time-of-flight (TOF) mass spectrometer. Note that in total ion yield a doubly ionized atom will result in twice the signal (current) than a singly ionized atom. Thus, total ion yield spectra do not always reflect the absorption cross section.

TOF spectrometers allow us to distinguish between the different charge states of the ions and, consequently, to measure the absorption cross sections separately for the differently charged final states of the photoionization process.

Note that the fluorescence decay channel of the core-excited atoms is not accounted for in photoabsorption experiments where ions are detected. This could, in principle, cause deviations of the spectra from the absorption cross section. However, in the energy region of the 3p and 2p excitation of 3d metal atoms up to several 100 eV as considered here the fluorescence decay has only a negligible contribution of less than 1% [107]. Hence, for the cases investigated here, photoabsorption spectra measured through ion detection to a good approximation reflect the absorption cross section. For some rare cases, when the Auger decay is forbidden due to selection rules such as in lithium [108], or when the Auger decay is strongly suppressed such as for some doubly excited states in helium [109, 110], the radiative decay channel can be dominant.

3.4. Photoelectron spectroscopy

With photoabsorption spectroscopy the unoccupied states of a system are probed. To get access to the full electronic structure of a system, also the occupied states have to be probed. One way to analyse the occupied states is photoelectron or photoemission spectroscopy (PES). In PES the energy distribution of the emitted photoelectrons is measured and it is assumed that the count rate is proportional to the density of occupied states (see, e.g., [111]). For developing the technique of high-resolution electron spectroscopy for chemical analysis (ESCA) K Siegbahn was awarded the Nobel prize in 1981. PES is now widely used to study the electronic properties of solids, liquids, surfaces and free atoms or molecules.

For photoionization of an unpolarized (unoriented) target by linearly polarized radiation and within the dipole approximation, the differential cross section is defined by Yang's [112] theorem:

$$\frac{\mathrm{d}\sigma}{\mathrm{d}\Omega}(\theta) = \frac{\sigma}{4\pi}[1 + \beta P_2(\cos\theta)] \tag{15}$$

Here θ is the angle between the polarization vector of the ionizing light and the momentum vector of the ejected electron. $P_2(x) = \frac{1}{2}(3x^2 - 1)$ is the second Legendre polynomial, and σ is the angle-independent cross section of the investigated ionization process. Detection of the photoelectrons at the so-called magic angle $\theta = 54.7^\circ$ relative to the polarization axis of the ionizing radiation results in a spectrum directly proportional to σ, since $P_2(\cos(54.7^\circ)) = 0$.

Every photoelectron spectrum shown in this review has been measured at the magic angle. Furthermore, only electrons emitted perpendicular to the propagation direction of the ionizing synchrotron radiation have been detected. Possible non-dipole effects in the angular distribution are thus eliminated [113–115].

To measure correlation effects using photoelectron spectroscopy high-resolution analysers are required. State-of-the-art resolution obtained in electron spectroscopy is of the order of 1 meV, using a hemispherical analyser with 200 mm radius for the electron path. In metal vapour experiments, the resolution is typically limited to a few 100 meV due to the low target density.

A different technique for PES uses time-of-flight (TOF) electron spectrometers (see, e.g., [116]). In principle, these spectrometers have the advantage that a certain kinetic energy range can be measured at once without scanning the spectrometer. Furthermore, they are easier and hence cheaper to build. An energy resolution in the order of 1 meV is achievable. However, an electron TOF spectrometer needs a well-defined starting pulse. Due to the typical time of flight of the electrons of the order of some 100 ns, a TOF cannot be used in the usual

multi-bunch operation mode of synchrotrons with a nanosecond typical time gap between the bunches. These spectrometers are suitable for the single, double or few bunch mode with much lower currents.

3.5. Experiments with free ions

Photoionization studies of free ions are scarce. The main problem for experiments with free ions is in most cases the low target density. Photoelectron spectroscopy of free ions is hampered by the large collisional cross section of ions with the residual gas in the UHV apparatus, which results in a strong electron background. Therefore only a limited number of photoelectron spectra of free ions exist [117–119].

Photoabsorption of free ions can be studied with the DLP method described above in section 3.3. High flux ion sources are also in operation at synchrotron radiation facilities such as the ALS (Berkeley, USA) and the Astrid storage ring (Aarhus, Denmark) [120–123]. In particular, photodetachment experiments with negative ions in the core level region have become possible for the first time [124–126]. In these experiments, an ion beam is merged over several 10 cm collinearly with the synchrotron light beam. This merged-beam technique was developed for collision experiments of atoms, ions and molecules with charged particle beams [127]. This technique allows absolute cross sections down to 0.1 Mb to be measured. A detailed description of the experimental methods used for free atomic ions and the results obtained are given in several review articles [128, 123, 129].

4. Photoabsorption spectroscopy of free 3d metal atoms

The first core level photoabsorption experiments on 3d metal atoms were performed by Mansfield and co-workers on Mn [130] and Cr [131] using synchrotron radiation and photographic plates. Sonntag and co-workers extended this work to the 3p–3d photoabsorption of the late transition metals Fe, Co, Ni and Cu using a heat pipe oven [132, 20, 133]. Furthermore, they performed the first photoemission experiments on these metals [21–23, 133]. Experiments on the early 3d metals were presented first by Schmidt [134]. A summary of these experiments is given in the review of Sonntag and Zimmermann [92].

Meyer *et al* [133] investigated the 3p–3d resonances in photoabsorption and photoemission. They found that the majority of the observed strong resonances can be attributed to 3p transitions into unoccupied 3d orbitals, i.e., $3p^6 3d^N \rightarrow 3p^5 3d^{N+1}$, with the subsequent emission of a 3d electron, i.e., $3p^5 3d^{N+1} \rightarrow 3p^6 3d^{N-1}\epsilon(p, f)$, as the main decay channel. Excitation as well as decay are governed by the large overlap of the 3p and 3d wavefunctions. For a quantitative analysis, it has to be taken into account that the coupling of the open 3d shell gives rise to a large number of discrete states that can interact with a correspondingly large number of continua. In addition, the 3d and 4s orbitals are nearly degenerate in energy resulting in strong configuration interactions of the type $(3d, 4s)^N$ with $3d^N$, $3d^{N-1}4s$, and $3d^{N-2}4s^2$.

4.1. 3p excitation

In figure 3 the experimental 3p photoabsorption spectra for the 3d elements are shown. A similar comparison has been presented in [92]. Here, however, new data for Sc [135], Ti [136], V [137] and Cr [138] are included. These latter measurements have been performed by measuring the partial ion yield with a TOF ion mass spectrometer. The photoabsorption signal is obtained by summing the spectra for the different ionization stages. Note that for 3p excitation only singly and doubly ionized atoms are created.

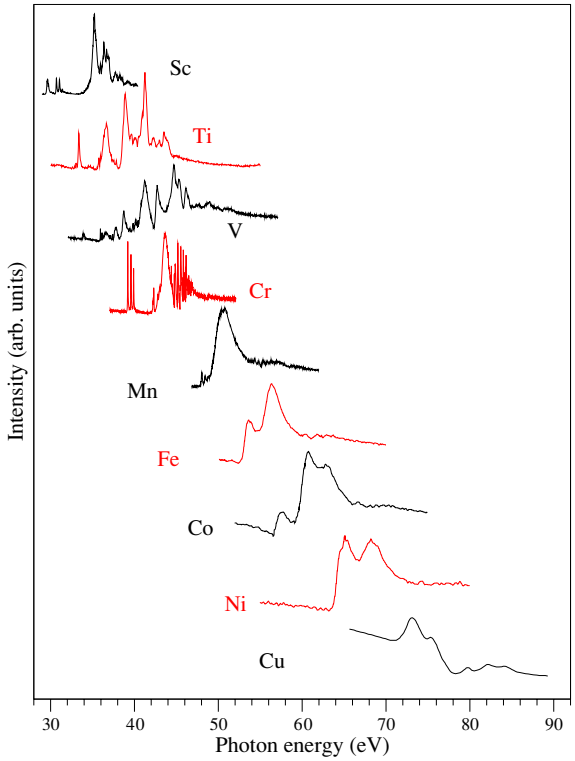

Figure 3. Experimental 3p photoabsorption spectra of the 3d metals in the region of the 3p–3d excitations. Data are taken from the following references: Sc [135], Ti [136], V [137], Cr [138], Mn [103], Fe, Co, Ni [139], and Cu [132].

In figure 4 the calculated 3p–3d absorption spectra are shown. The calculation for Cr, performed by Dolmatov, shows only the main 3d channel and has been taken from [35]. A similar calculation for Cr was presented by Donnelly *et al* [85] using the R-matrix method with a similar result. For all other elements the spectra have been calculated using the extended Fano formalism described in section 2.3 and in [28]. CI is included in the ground, intermediate and final states of the photoionization process. In all spectra, the thermal population of the initial states has been taken into account, where needed (see table 3).

The agreement of calculated and measured 3p–3d photoabsorption spectra is excellent for the late 3d elements Fe, Co and Ni. For the earlier 3d elements Sc, Ti and V there are only clear similarities between theory and experiment.

From Mn to Ni the spectra are dominated by strong, broad resonances, which are due to the 3p $\rightarrow$ 3d excitation; these are often denoted the 'giant resonances' of the 3d elements. For Cu this resonance is missing and the spectrum shows only weak modulations because the 3d shell is closed. With laser radiation a Ni-like Cu configuration $3d^9 4s^2$ with one 3d hole has been prepared by exciting the Cu 4s electron into a 4p state. This $3d^{10}4p$ state can decay into the Ni-like configuration $3d^9 4s^2$. Photoionizing this laser-tailored Cu state results also in a broad 3p–3d resonance similar to the other late 3d elements [142].

As can be seen from figure 3 the 3p photoabsorption spectra of Cr and Mn are quite different. The Mn spectrum is similar to the spectra of the heavier elements with one broad resonance and some fine structure, whereas for Cr pronounced Rydberg excitations into nd

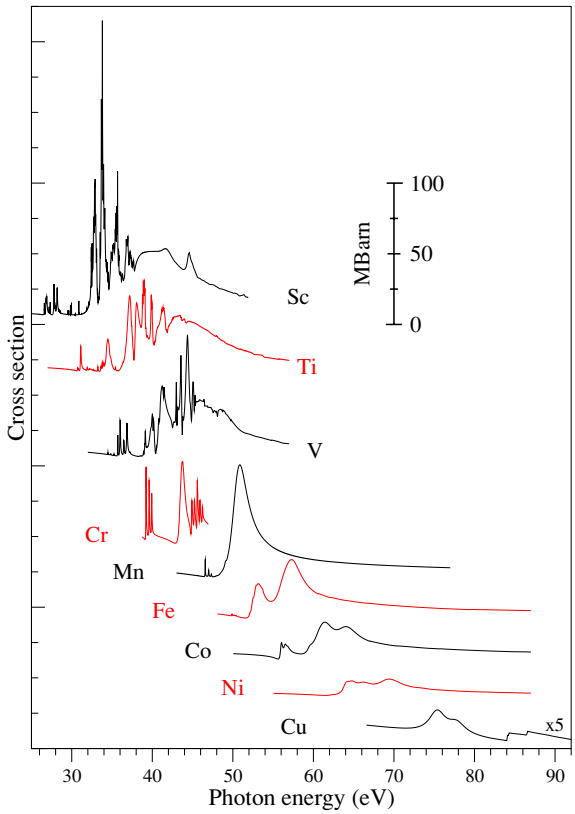

Figure 4. Theoretical 3p photoabsorption spectra of the 3d metals in the region of the 3p–3d excitations. The Cr spectrum has been calculated by Dolmatov and is taken from [35]. All other spectra have been calculated using the extended Fano formalism described in section 2.3 (Sc [140], Ti, V, Mn, Cu [141], and Fe, Co, Ni [139]). The cross sections have been stacked so as not to have overlapping spectra, while the scale is untouched. For Cu, the cross-section scale was magnified by a factor of 5.

states are observed. The three sharp lines around 40 eV photon energy are due to 3p $\rightarrow$ 4s excitations which are possible only for Cr, as a result of the half-filled 4s shell.

For Cr and Mn several calculations were published. Due to their half-filled 3d shell several powerful methods like the SP-RPAE (spin-polarized RPAE) method [83, 143–154] or the R-matrix method [83–86] have been applied and resulted in good agreement with the experimental data.

The spectra of Sc, Ti and V are more complicated. A large number of comparably sharp resonances are observed but no clear Rydberg structure can be found from a theoretical point of view, because only one electron is added in comparison to Ca with its closed shells. Sc can thus be regarded as a prototype case for studying open shell atoms.

4.1.1. The early elements (Sc, Ti, V). Scandium with the ground state $4s^2 3d\,^2D$ is the simplest 3d element. The valence shell excitation of Sc has been analysed by Robicheaux *et al* in a series of three papers [155–157]. They were able to describe the photoabsorption in the wavelength range from 170–190 nm (6–7 eV) in great detail using eigenchannel R-matrix calculations.

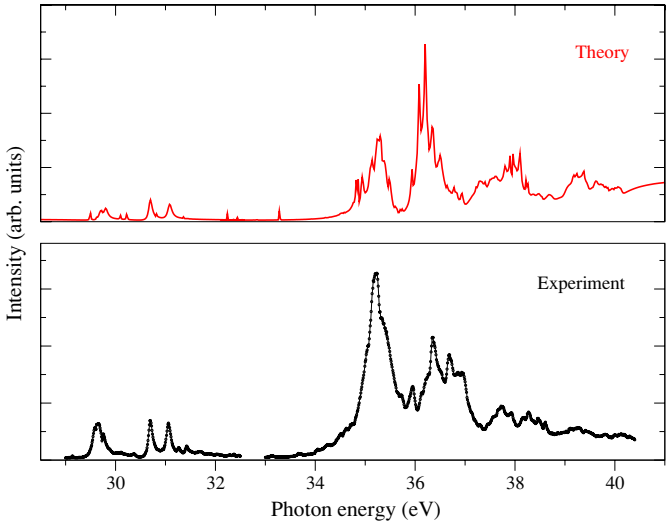

Figure 5. Comparison of the experimental and theoretical Sc 3p → 3d photoabsorption spectra. The experimental data of Whitfield *et al* [135] include only the 3d and 4s partial cross sections. The calculation [140] is the total cross section, including the 3p channel.

The first theoretical analysis of the 3p photoabsorption spectrum came from Altun and Manson [66–68, 158] based on the many-body perturbation theory (MBPT), the close-coupling approximation and the multi-configuration Hartree–Fock (MCHF) approach. However, as Whitfield *et al* [135, 159] showed, there is only a marginal agreement between experiment and theory. Compared to valence excitations the 3p–3d excitation is much more complex. The 3p core hole induces strong correlations of the valence electrons (3d, 4s, 4p), which result in a breakdown of the single configuration approximation. In figure 5 the experimental data of Whitfield *et al* [135] are compared to a calculation [140] based on the extended Fano theory. This calculation, which includes strong correlations due to the 3p hole and the spin–orbit coupling, shows some agreement with experiment. Altun and Manson included correlations as well, but their basis set was possibly not large enough. For the valence electrons on the other hand, a single configuration approximation is sufficient and therefore the model of Robicheaux and co-workers successfully described the experimental data.

In a simple picture, the Sc ground state can be described by the spin of the 3p and 3d electrons as $(\uparrow\uparrow\uparrow\downarrow\downarrow\downarrow)_{3p}\uparrow_{3d}$; the 4s electrons are not taken into account. Spin-up ↑ and spin-down ↓ 3p electrons can thus be excited into the unoccupied 3d orbitals resulting in ^1L and ^3L parent states for $3d^2$. Such an excitation is also possible for Ti and V with a less than half-filled 3d shell.

In table 4 the energy, the line strength S_{ik} and the line width Γ of the strongest $3p^5 3d^2 4s^2$ resonances for the initial state $^2D_{3/2}$ are given. The $3p^5 3d^2 4s^2$ main resonances are clearly separated into two energy regions around 30 eV and 42 eV. These regions can be assigned to states with mainly $3d^2$ (^3L) and $3d^2$ (^1L) parent terms, respectively. In the second region, the effective 3p spin and the spin of the 3d electrons are oriented anti-parallel, whereas in the first region their orientation is parallel. The 3p–3d Coulomb exchange interaction is different for the two regions and their energy separation can be explained by the large exchange interaction integral G^1(3p, 3d). This effect is also discussed in relation to the 3p photoelectron spectra in section 5.1.

Table 4. Resonances of the Sc 3p–3d excitations taken from [140]. The resonance energy $h\nu$, the line strength S_{ik} and the width Γ of only the main resonances belonging to the configuration $3p^5 3d^2 4s^2$ are shown. In the last columns, the spins of the 3p core hole and the 3d electrons are given. The strong resonances at 34–38 eV are discussed in the text and not included in this table.

				Spin	
State	$h\nu$ (eV)	S_{ik} (ea_0)	Γ (eV)	$3p^{-1}$	3d
$(^3F)^4F_{3/2}$	29.600	0.103	0.012	↑	↑↑
$(^3F)^4F_{5/2}$	29.604	0.100	0.014	↑	↑↑
$(^1G)^2F_{5/2}$	29.792	0.372	0.089	↑	↑↓
$(^1D)^2P_{1/2}$	30.196	0.133	0.017	↑	↑↓
$(^1D)^2F_{5/2}$	31.178	0.517	0.095	↑	↑↓
$(^3P)^2P_{1/2}$	41.513	1.233	4.1	↓	↑↑
$(^3P)^2P_{3/2}$	41.603	0.700	5.7	↓	↑↑
$(^3F)^2D_{5/2}$	42.118	0.714	5.7	↓	↑↑
$(^3F)^2D_{3/2}$	42.126	2.558	7.4	↓	↑↑

For Fe and the other late transition metal atoms the situation is different. The spins of the 3p and 3d electrons in the ground state are given by $(\uparrow\uparrow\uparrow\downarrow\downarrow\downarrow)_{3p}(\uparrow\uparrow\uparrow\uparrow\uparrow\downarrow)_{3d}$. In contrast to the early elements only spin-down ↓3p electrons can be excited into the unoccupied 3d orbitals, because the 3d↑ orbitals are already filled. Compared to Sc, only states of one region can thus be excited because the spin cannot be changed in a dipole transition in the simple one-electron picture. This results in a smaller number of resonances and hence in a much simpler spectrum.

There is, however, another important reason for the complex structure of the Sc 3p absorption. The dominating resonances around 34–38 eV in figure 5 originate from the configurations $3p^5 3d^2 4p^2$ and $3p^5 3d 4s^2 4d$ [140], not listed in table 4. They are excited by the strong configuration interaction with $3p^5 3d^2 4s^2$. This CI comes from the near degeneracy of the 3d and 4s orbitals. This degeneracy is more pronounced for the earlier 3d elements than for the later ones.

The photoabsorption of Sc^{2+} and the photorecombination process of Sc^{3+} have also attracted attention [66, 90], because Sc^{2+} has a similar initial state as the Sc atom with one 3d electron. The photorecombination process

$$Sc^{3+} + e^- \rightarrow Sc^{2+} + h\nu \tag{16}$$

can be understood as the reversed process of photoionization described by equation (5). The detailed balance of both processes is very important for, e.g., the description of hot plasma environments, as found in controlled fusion or astrophysics. The Sc^{2+} and Sc^{3+} ions offer the opportunity to compare the photoionization and the photorecombination processes. Schippers *et al* reported a strong 3d → 3p radiative decay of $3p^5 3d^2$ and $3p^5 3d\,4s$ photorecombination resonances [160, 161]. A comparison of these experimental data and of the theoretical spectrum of Altun and Manson [66] for Sc^{2+} shows only marginal agreement again. Hence, also for Sc^{2+} the 3p core hole induces strong correlations as in the Sc atom.

To date no experimental or theoretical vanadium core level photoabsorption data have been reported and for titanium only the experimental data published by Sonntag and Zimmermann are known [92]. The scarcity of experimental data is most probably due to the very high evaporation temperatures needed for appropriate target densities for these elements (see table 3). Note that investigations of valence excitations using a helium gas discharge lamp have been reported [162].

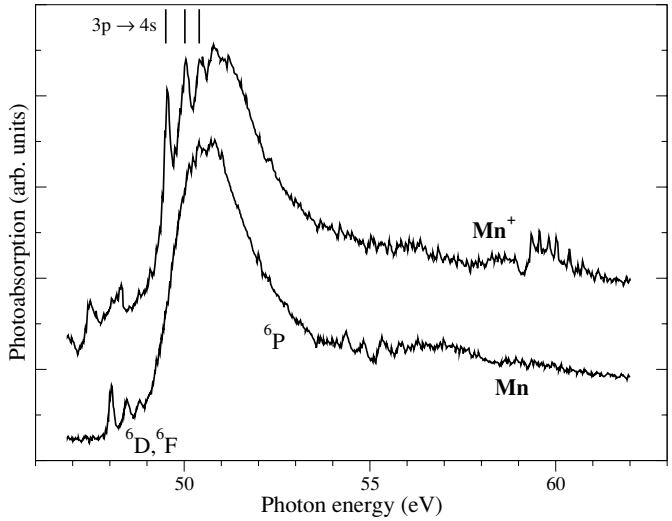

Figure 6. Photoabsorption of Mn atoms and singly ionized Mn taken from [103].

Table 5. Configurations included in the calculations of the Ti and V 3p–3d photoabsorption spectra.

	Initial state	Resonant state	Continua
Ti	$3d^24s^2$, $3d^34s$, $3d^4$, $4s^24p^2$, $3d4s^24d$	$3p^53d^34s^2$, $3p^53d^44s$, $3p^53d^5$, $3p^53d^24s^24d$, $3p^53d4s^24p^2$	$3d4s^2$, $3d^24s$, $3d^3$, $4s4p^2$, $4s^24d$, $3d4s4d$, $3d^24d$ $4s^24p$, $3d4s4p$, $3p^54s^23d^2$ $3p^54s\,3d^3$, $3p^53d^4$, $3p^54s^24p^2$
V	$3d^34s^2$, $3d^44s$ $3d^5$, $3d^34p^2$	$3p^53d^44s^2$, $3p^53d^54s$, $3p^53d^6$, $3p^53d^44p^2$, $3p^53d^34s^24d$, $3p^53d^44s4d$, $3p^53d^34s^25s$, $3p^53d^44s5s$	$3d^24s^2$, $3d^34s$, $3d^4$, $3d^24p^2$, $3d^34d$, $3d4s^24d$, $3d^24s4d$, $3d^35s$, $3d4s^25s$, $3d^24s5s$, $3p^53d^34s^2$, $3p^53d^44s$, $3p^53d^5$

The 3p photoabsorption spectra of Ti and V are similar to that of Sc. Calculations are even harder to perform than for Sc due to the increased number of 3d electrons. In order to keep the size of the energy matrices manageable a smaller configuration set as indicated in table 5 was used here in the CI calculations for Ti and V.

V is probably the most complex atom of the light 3d elements and to date theory can give only a qualitative description of the 3p–3d photoabsorption spectrum. At an evaporation temperature of 2100 K two different initial configurations, namely $3d^34s^2$ and $3d^44s$ (see table 3) are thermally populated. This leads to a large number of configurations (see table 5) that have to be included in the calculations.

4.1.2. Chromium and manganese. Cr and Mn are the theoretically and experimentally best investigated atoms of the 3d metals in the gas phase. In particular from a theoretical point of view, they are simpler due to the half-filled 3d shell. Experiments are also much easier to perform, due to the relatively low evaporation temperatures (see table 3). In addition, studies of free Cr and Mn ions have been reported and photoionization experiments on laser-excited Cr atoms have been performed.

In figure 6 the spectra of atomic Mn and of Mn^+ ion are shown. Both spectra are similar and well understood. The main resonance is due to the 3p → 3d excitations and can be

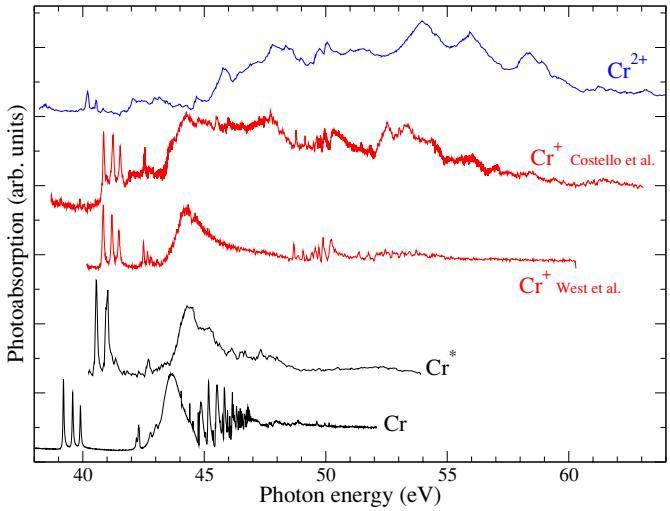

Figure 7. Photoabsorption of Cr atoms, laser-excited Cr* [163] and Cr ions. For Cr^+ the data of Costello *et al* [103] and the more recent data of West *et al* [164] are shown. The high-resolution spectrum of atomic Cr is taken from [138].

assigned to ^{6}P states. The small pre-edge lines in the Mn 3p–3d spectrum can be assigned to ^{6}D and ^{6}F states with a recoupled $3d^5$ shell. For Mn^+ in addition the 3p → 4s excitations are observed at similar energies as the 3p → 3d resonances. However, in contrast to Cr with the same ground state $3d^54s\ ^7S_3$ the Rydberg excitations at higher energies are missing in the Mn^+ spectrum. This is addressed below. Compared to Cr also the line widths of the ^{6}P main resonances and of the ^{6}D and ^{6}F pre-peaks are different.

These latter differences have been explained by Davis and Feldkamp [65]. The line width $\Gamma_{^6P}$ of the ^{6}P resonance is a result of the large super-Coster–Kronig (SCK) CI radial integral $R^1(3d^2, 3p\epsilon f)$. For the ^{6}D resonance the corresponding angular coefficient $r_{1,^6D}(3d^2, 3p\epsilon\ell)$ of the SCK channel vanishes, resulting in a much smaller line width $\Gamma_{^6D}$. This is a consequence of rotation and inversion symmetry. The line width $\Gamma_{^6F}$ of the ^{6}F state is much smaller than $\Gamma_{^6P}$, because $\Gamma_{^6L} \propto (2L+1)^{-4}$ [65]. Note that these effects also explain the different line widths of the 3p–3d resonances for the early 3d elements Sc, Ti and V.

The analysis of the Cr 3p photoabsorption spectrum has been a problem for some time, in particular since the spectrum of Mn^+, with the same ground state $3d^54s\ ^7S_3$, looks completely different. Figure 7 shows the 3p–3d photoabsorption spectra of Cr atoms, Cr ions and laser-excited Cr*. The Cr* spectrum has been measured by laser-exciting the Cr 4s $^7S_3$ ground state to the Cr* $3d^54p\ ^7P_4$ state [163]. There are striking differences between these and the Mn spectra in figure 6.

A first successful description of the Cr spectrum was given by Dolmatov using the spin-polarized Hartree–Fock method (SPHF) [165] and the spin-polarized random phase approximation with exchange (SP-RPAE) [152, 144]. The particular behaviour of Cr could be attributed to a spin-dependent anti-collapse of the 3d wavefunction. A similar result for the Cr 3p–3d photoabsorption spectrum was obtained by Donnelly [85] *et al* using the R-matrix theory. The SP-RPAE is based on SPHF wavefunctions, which is essentially the unrestricted HF method. Figure 8 shows the 3d↓ wavefunctions of Mn and Cr for 3p core hole states calculated using a frozen core and a relaxed SPHF calculation [152]. In the Cr ground state $3d^54s\ ^7S_3$ all 3d↑ orbitals are occupied, so 3p electrons can only be excited into 3d↓ orbitals.

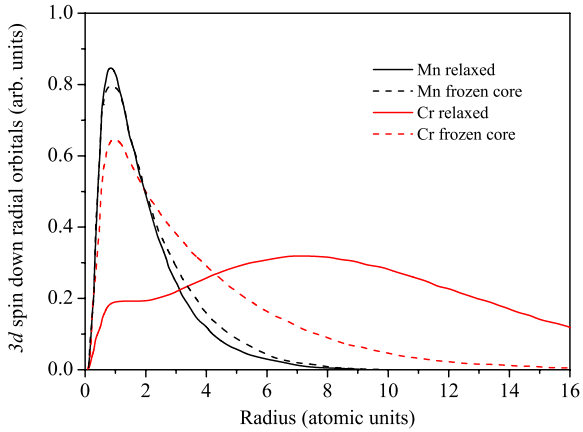

Figure 8. Radial 3d↓ wavefunctions from two different SPHF calculations for 3p core-excited Mn and Cr. The calculation has been taken from [152].

In a restricted HF and in the frozen core SPHF calculation the 3p core-excited Cr 3d↓ orbitals have almost the same shape as for Mn. However, if the relaxation of the 3d orbitals in the 3p core hole configuration is taken into account an anti-collapse of the Cr 3d↓ orbitals is observed [152].

This anti-collapse of the wavefunction is extremely sensitive to the nuclear charge Z of the atom and is only observed for Cr atoms in their ground state. Already for laser-excited Cr^* [166, 163] the 3p photoabsorption spectrum is similar to that of manganese. The Rydberg series vanish and the spectrum becomes similar to that of Mn and Mn^+. This can be understood by considering that the 4p wavefunction of excited Cr^* has a lower probability for small radii than the 4s wavefunction. Hence the core potential is less screened for the 3d electrons, the anti-collapse of the 3d wavefunction does not occur [163].

The spectra of Cr^+ and Cr^{2+} in figure 7, which were experimentally observed for the first time using the DLP method [102, 103], are completely different compared to the Cr, Cr^*, Mn and Mn^+ spectra. For Cr^+ and Cr^{2+} the 3p → 3d photoabsorption resonances extend over more than 15 eV, which is about three times more than the 4–5 eV energy range of the atomic Cr and Mn resonances. First calculations by Dolmatov [167] and Donnelly *et al* [84] using the SP-RPAE and R-matrix method, respectively, were not successful at describing the experimental data. Therefore, extended Fano calculations were performed, which are in good agreement with the photoabsorption spectra measured with the DLP method [105, 168]. For investigations of Cr ions with the DLP method the main problem is the large number of metastable states populated in the laser plasma. In Cr^+ about 40 possible states belonging to the $3d^5$ and $3d^4 4s$ configurations exist below the first $3d^4 4p$ state. These states cannot decay via dipole radiation and hence excitations from all these metastable states have to be taken into account in the calculation of the photoabsorption cross section. In a first approach, the population according to a thermal or Boltzmann distribution has been assumed with a plasma temperature around 1.5 eV resulting in a reasonable agreement with the experimental data [105]. For Cr^{2+} a similar result is obtained for a plasma temperature of about 3 eV [168]. Here excitations from the $3d^4$ configuration are dominating the spectrum.

Recent experimental results for the Cr^+ photoionization cross section of West *et al* [164] show a much simpler spectrum, which is in good agreement with the theory of Dolmatov and Donnelly [167, 84]. West *et al* have recorded the Cr^+ spectrum using the merged ion beam

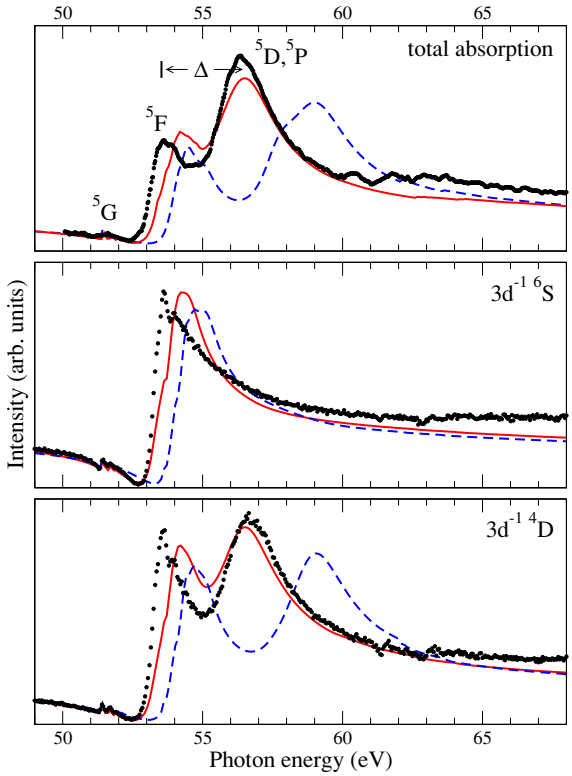

Figure 9. Comparison of calculations for the 3p photoabsorption of free Fe atoms. Dotted black curves are experimental data for total cross section (upper panel), partial cross section for the Fe II $3d^54s^2$ final states ^{6}S (middle panel) and ^{4}D (lower panel). The theoretical curves are calculated with (solid), and without (dashed) the influence of the $3d \rightarrow \epsilon\ell$ and $3p \rightarrow \epsilon\ell$ continua. The experimental data (points) are taken from [169], theoretical curves from [141]. Theoretical spectra have been shifted to match the experimental data. Δ is the energy splitting between the Fe main resonance ^{5}F and ^{5}D, ^{5}P.

technique at the Astrid storage ring for synchrotron radiation in Aarhus (see section 3.5). Using this method they were able to measure the spectrum of a comparatively cool ion beam, avoiding metastable states. In turn, these data are an excellent proof of the interpretation in terms of excitations from metastable states in the hot plasma [105].

4.1.3. The late elements (Fe, Co, Ni, Cu). The photoabsorption spectra of the heavier elements are all rather similar. They all show some broad resonances with very little fine structure and no Rydberg excitations [139].

Meyer *et al* [133] systematically investigated these resonances in absorption and photoelectron emission. A detailed analysis of the photoionization process by photoion spectroscopy is given in [139] using TOF mass spectra and CI calculations.

In contrast to the earlier elements with their strong CI, for the late 3d elements already SCA calculations result in good agreement with the experimental data. This is demonstrated for Fe in figure 9. In the SCA calculation only the configurations $3p^63d^64s^2$ and $3p^53d^74s^2$ have been included for the initial and intermediate states, respectively, whereas for the CI calculation the configurations $3d^64s^2$, $3d^74s$ and $3d^8$ for the ground state and $3p^53d^74s^2$, $3p^53d^84s$ and $3p^53d^9$ for the final states have been used. The difference between the theoretical Fe spectra

Table 6. Shifts F_k for the Fe 3p → 3d main resonances and the ^{5}G pre-peak due to the interactions with the continua.

	F_k (eV)		
	3d → $\epsilon\ell$	3p → $\epsilon\ell$	Sum
^{5}G	−0.1	−0.4	−0.5
^{5}F	−0.4	−0.7	−1.1
^{5}D	−1.3	−1.7	−3.0
^{5}P	−0.9	−1.5	−2.6

is negligible and therefore only the SCA calculation is shown in figure 9. Note that a further inclusion of the $3d^6 4p^2$ and $3p^5 3d^7 4p^2$ configurations only results in a energy shift of the whole resonance structure. The overall shapes of the experimental and theoretical spectra of the late 3d elements are in good agreement but the experimentally observed splittings Δ of the main resonances (like ^{5}F–^{5}D, ^{5}P for Fe) are overestimated in both the SCA and the CI calculations.

This splitting can be nicely studied in the resonant 3p → 3d photoemission, which has been investigated by Meyer *et al* [133] and Whitfield *et al* [169]. They measured the 3d partial cross sections in the region of the 3p → 3d giant resonances using photoelectron spectroscopy. In figure 9 the experimental spectra of the final ionic channels $3d^5 4s^2$ ^{6}S and $3d^5 4s^2$ ^{4}D are compared to spectra calculated within the extended Fano approximation (see section 2.3 and [75]). For the $3d^{-1}$ ^{6}S channel only an excitation into ^{5}F states is found. In the $3d^{-1}$ ^{4}D channel excitations into the ^{5}F and the ^{5}D, ^{5}P resonances are observed. Experimental and theoretical spectra are similar, but the calculated splitting $\Delta_{\text{theo}} \cong 4.4$ eV between the ^{5}F and the ^{5}D, ^{5}P resonances is too large compared to the experimental value $\Delta_{\text{exp}} \cong 3.1$ eV.

The key to understanding this shift is the interaction of a resonance with continuum states. In the Fano theory [62] the energy position of a resonance k is given by $E_k = E_{0,k} + F_k$ with

$$F_k = \mathcal{P} \int \frac{V_k(\epsilon)^2}{\epsilon - E_{0,k}} \, \mathrm{d}\epsilon. \tag{17}$$

$\mathcal{P}$ denotes the principal value; $E_{0,k}$ is the unperturbed resonance position. Usually this term is neglected, because for a resonance k embedded in a flat, weakly interacting continuum the Coulomb interaction $V_k(\epsilon) = \langle \Psi^k | \mathcal{H}_{\text{Coul}} | \varphi(\epsilon) \rangle$ between the resonance k and the continuum $\varphi(\epsilon)$ is independent of ϵ and F_k tends to zero. However, if $V_k(\epsilon)$ depends strongly on the energy ϵ or the resonance is close to a threshold, F_k cannot be neglected [28].

This has been found, for example, for the Mn 3p → 3d ^{6}P giant resonance by Davis and Feldkamp [65]. They calculated a shift of $F_{^6\text{P}} \cong -2.2$ eV due to the strong interaction of the $3p^5 3d^6 4s^2$ ^{6}P resonant state with the $3d^4 4s^2 \epsilon\ell$ (3d → $\epsilon\ell$) continuum.

For the neighbouring element Fe a similar shift can be expected. However, there it has to be calculated for the three main resonances ^{5}F, ^{5}D and ^{5}P independently. In table 6 the shifts due to the interactions with the 3d → $\epsilon\ell$ continuum are listed for the three main resonances and the weak ^{5}G pre-peak. All of them are smaller than for Mn. More importantly, the shifts are larger for the ^{5}D and ^{5}P states than for the ^{5}F and ^{5}G states leading to a smaller splitting Δ. However, the calculated splitting $\Delta_{(3d\epsilon\ell)} \cong 3.8$ eV is still too large, as compared to the experiment.

In the work of Fano [62] the interaction of a resonance with continuum states is taken into account for the case, where the resonance is embedded in the continuum. If the integral (equation (17)) is generalized to continua, where the resonance is not embedded in, the

resonance will also be shifted towards smaller excitation energies. Therefore, in table 6 also the calculated shift F_k due to the influence of the $3p \rightarrow \epsilon\ell$ continuum is listed. Including the interaction with the $3p \rightarrow \epsilon\ell$ continuum reduces the splitting further to $\Delta_{(3p\epsilon\ell)} \cong 2.6$ eV.

In figure 9 the theoretical spectra without the shift F_k (dashed line) and including the shifts due to the $3d \rightarrow \epsilon\ell$ and the $3p \rightarrow \epsilon\ell$ continua (solid line) are shown for the two channels ^{6}S and ^{4}D in comparison with the experimental data of Whitfield *et al* [169]. The energy scale of the theoretical spectra have been adjusted to the weak ^{5}G pre-peak; for this peak a much smaller shift $F_{^5\mathrm{G}}$ is obtained [65].

In the ^{6}S channel an improvement in the energy position of the ^{5}F resonance relative to the ^{5}G pre-peaks is found, when the interaction with the continua is taken into account. However, this effect is quite small. A major improvement is found for the ^{4}D channel. Including the interaction with the $3d \rightarrow \epsilon\ell$ continua already shows better agreement with experiment, while the energies of the main resonances remain too large. If also the interaction with the $3p \rightarrow \epsilon\ell$ continua is included almost perfect agreement with the experimental data is obtained. Thus, the strong interaction with the continuum states causes the large shift of the order of several eV for some of the $3p \rightarrow 3d$ resonance positions in Fe and also for Co and Ni [139] and Mn [65].

4.2. The 2p excitation

Studies of the 2p excitation of the 3d transition metal atoms Cr, Mn and Cu were done first by Arp *et al* [170–173] in the 1990s. For the other 3d elements such experiments have been accomplished in recent years due to the increased photon flux at third-generation synchrotron radiation sources.

In figure 10 the experimental 2p photoabsorption cross sections in the energy region of the 3d excitations are shown. In contrast to the 3p–3d resonances the 2p–3d resonance energies of the different elements do not overlap and the 2p–3d excitations are highly element specific. The 2p–3d excitations are hence an excellent tool for the study of electronic and magnetic properties of complex 3d metal compounds and thin films [18, 177–181].

Figure 11 displays spectra calculated with the Fano method (see section 2.3). Overall there is good agreement with the experimental data. The Fano theory is usually sufficient to calculate the photoabsorption spectra, because the resonances are mostly isolated and the effect of overlapping resonances is quite small. The 2p photoabsorption is dominated by two groups of lines, which can be assigned in a first approximation to $2p_{3/2}^{-1}$ and $2p_{1/2}^{-1}$ spin–orbit split core hole states. Coulomb interaction of the 2p core hole with the 3d electrons gives rise to an additional multiplet splitting for both the $2p_{3/2}^{-1}$ and the $2p_{1/2}^{-1}$ states. It is apparent from both figures 10 and 11 that the spin–orbit splitting increases with increasing nuclear charge Z from 5 eV for Sc to 20 eV for Cu. For the early elements, there is still a partial overlap of $2p_{3/2}^{-1}$ and $2p_{1/2}^{-1}$ states [174], due to the smaller 2p spin–orbit splitting. This might have consequences for the validity of sum rules in the analysis of XMCD spectra [182, 183]. Note that for Cu the 2p resonances are comparably weak due to the closed 3d shell.

The first theoretical analysis of the Cr and Mn 2p photoabsorption spectra using SCA calculations was presented by Arp *et al* [172, 170, 173]. It was shown that the main features of the spectra can be explained within the SCA. Rydberg excitations or, more generally, electron correlations are only of minor importance. The situation changes slightly for Sc, as has been shown in [174]: Due to the overlap of the $2p_{3/2}^{-1}$ and $2p_{1/2}^{-1}$ multiplets excitations into 4d Rydberg orbitals have to be included.

In the calculations by Arp *et al* the lifetime of the resonances due to the subsequent Auger decay of the 2p core hole states was included (Lorentzian line widths of 0.339 eV and

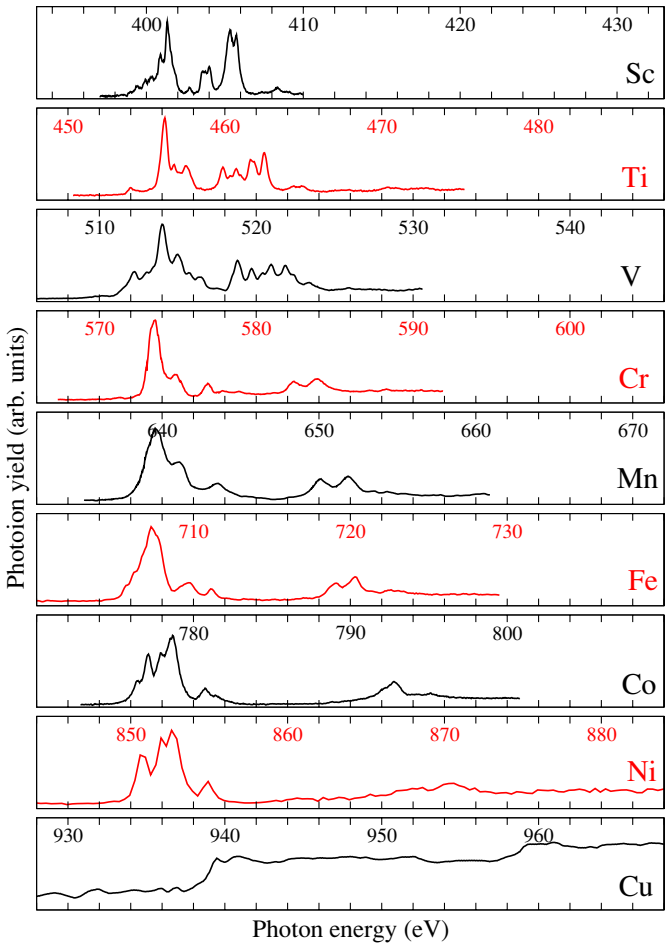

Figure 10. Experimental 2p photoabsorption spectra of the 3d elements. The spectra cover the same energy range of 40 eV. Data are taken from the following references: Sc [174], Ti, V [175], Cr [172], Mn [170], Fe [38], Co [176], Ni [37] and Cu [171].

0.392 eV for the Mn $2p_{3/2}^{-1}$ and $2p_{1/2}^{-1}$ core hole states, respectively, have been used [61]). For the other 3d elements the lifetime broadening has been calculated by van der Laan *et al* [184] to increase from 200 meV for Sc to 500 meV for Ni. In figure 11 the line width has been calculated by taking into account the subsequent Auger decay of the 2p core hole. Sc 2p holes mainly decay via an Auger process to $3p^{-2}$ which results in Sc^{3+} ions [174, 185]. To keep the number of final ionic states for the calculations manageable only this main decay channel and the $3d^{-2}$ and $3p^{-1}3d^{-1}$ decay channels are included. This results in a typical line width of 0.2–0.3 eV for the $2p_{3/2}^{-1}$ core hole states. With this approach the line width is underestimated because other decay channels are neglected. The $2p_{1/2}^{-1}$ states show a stronger broadening of 0.4–0.5 eV as can be seen in figure 12 for the case of Ni. This is due to an additional spin-flip decay channel possible for the $2p_{1/2}^{-1}$ core hole states, as they are located above the $2p_{3/2}^{-1}$ threshold.

Arp *et al* already pointed out that the electronic structure of the 2p excited 3d transition metals have to be described in intermediate coupling, because the 2p spin–orbit parameter

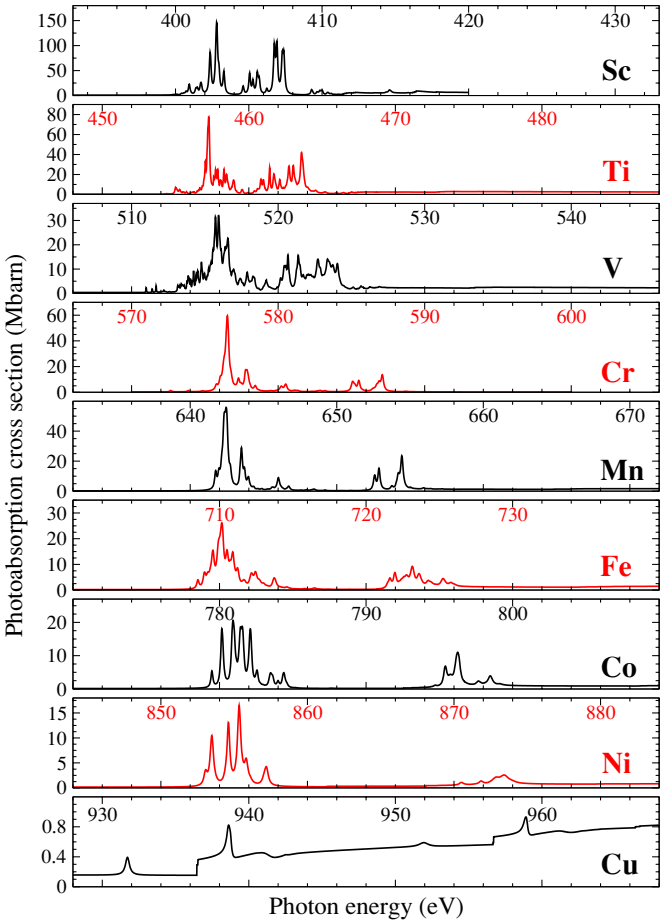

Figure 11. Theoretical 2p photoabsorption spectra of the 3d elements. The spectra have been calculated within the SCA taking into account the thermal population of the initial states for Sc, Ti, V and Ni. For Sc an additional 4d Rydberg excitation is included. The displayed energy ranges are the same for all spectra and they are the same as for the experimental data in figure 10. Spectra are reported without any energy shifts applied. Calculations are taken from the following references: Sc [174], Ti, V, Cr, Mn [141], Fe [38], Co [176], Ni [37] and Cu [141].

ζ_{2p}, and the Slater integrals $F^k(2p3d)$, $F^k(3d3d)$, $G^k(2p3d)$ are of similar magnitude (several eV). This will be further investigated below.

In [37] the 2p photoabsorption of atomic Ni has been presented. Ni, like the other late 3d metal atoms, can be well described within a SCA. As for V, the excitation from two different thermally populated ground states has to be taken into account. In figure 12 the 2p photoabsorption is shown for both initial configurations, $3d^84s^2$ and $3d^94s$. The latter contributes only with one strong line ($^3P_2$) to the spectrum due to selection rules. For condensed matter systems several authors [186–188] have shown that the initial state has to be described in a CI expansion including $3d^8\underline{L}^2$, $3d^9\underline{L}$ and $3d^{10}$ configurations; $\underline{L}$ denotes a valence electron of the ligand. In particular in Ni metal the 6 eV satellites of the $2p_{3/2}^{-1}$ lines in x-ray absorption and photoemission spectra [189] result from electron correlations in the solid. Here the atomic data can be helpful to assign resonances in solid systems to an initial state configuration. The influence of different symmetries on the 2p photoabsorption in solids,

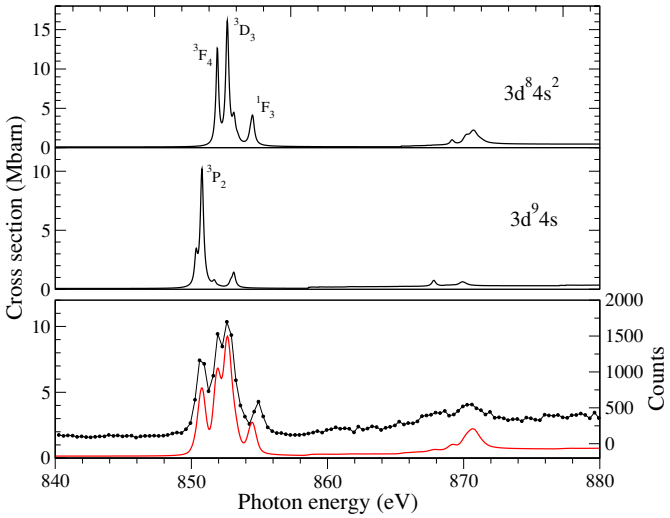

Figure 12. 2p photoabsorption of atomic Ni for the $3d^84s^2$ and $3d^94s$ configuration. The lower panel compares the experimental data [37] (dots) with the sum of the spectra (solid line) of the initial two configurations weighted according to their thermal population.

and here in particular in 3d metal compounds, has been studied by van der Laan [184] and de Groot [178] for several ligands. The influence of the crystal field on the absorption spectra was demonstrated. However, the term-dependent decay of the 2p core hole has been neglected.

4.3. Comparison of the 3p and 2p photoabsorption

In contrast to the 3p excitations, where the photoabsorption spectrum of the early elements is dominated by strong correlation effects, the 2p photoabsorption can be successfully described within a SCA. This is somewhat surprising, because there are only small differences between the CI integrals R^k (equation (4)) of the 3p hole configurations and the corresponding 2p configurations (table 7); the 2p CI integrals are on average about 10–20% smaller than the 3p CI integrals. Also the difference between the average energy E_{av} of the configurations is comparable for a 2p and a 3p hole configuration. However for the spin–orbit interaction, one finds

$$\zeta_{2p} \approx 8 \cdot \zeta_{3p}. \tag{18}$$

This much larger 2p spin–orbit interaction as characterized by ζ_{2p} distributes the states over a larger energy range. As a consequence, the energy separation between interacting states increases, and the mixing of these states as described by second order perturbation theory decreases. As a result correlations are less important.

In table 7 CI integrals R^k are given, where only electrons from the valence shell (4s, 4p or 3d) are involved. The CI integrals, where also the core hole electrons are involved, e.g., R^2(2p4s, 2p3d), have smaller values approximately 10–20% of the tabulated CI integrals.

The simplicity of the 2p photoabsorption spectra can also be explained by the smaller line width of the 2p as compared to the 3p resonances. The 3p resonances can be very broad with line widths up to several eV, due to the super-Coster–Kronig (SCK) decay of the 3p core hole. Therefore, the 3p spectra have to be described using the extended Fano theory, taking into account interference effects of the overlapping resonances. In contrast, for the 2p hole there

Table 7. CI integrals and average energies E_{av} of several 2p and 3p core hole configurations for Sc, Cr and Co. E_{av} is given relative to the $[2p, 3p]^5 4s^2 3d^n$ configuration of each element. Only CI integrals which include the valence electrons are given in the table.

	E_{av} (eV)			CI integrals R^k (eV)		
	$3p^5$	$2p^5$			$3p^5$	$2p^5$
Sc	1.469	0.672	$4s3d^3$	$R^2(4s3d, 3d^2)$	−1.30	−0.92
	4.767	3.892	$3d^4$	$R^2(4s^2, 3d^2)$	1.96	1.76
	11.442	15.738	$4s^24p^2$	$R^1(3d^2, 4p^2)$	1.29	1.09
				$R^3(3d^2, 4p^2)$	0.99	0.87
	5.384	5.357	$3d^24p^2$	$R^1(4s^2, 4p^2)$	3.65	3.72
Cr	0.673	−0.197	$4s3d^6$	$R^2(4s3d, 3d^2)$	−0.83	−0.54
	4.210	3.172	$3d^7$	$R^2(4s^2, 3d^2)$	1.65	1.48
	17.018	21.164	$3d^34s^24p^2$	$R^1(3d^2, 4p^2)$	1.08	0.96
				$R^3(3d^2, 4p^2)$	0.85	0.77
	6.692	6.594	$3d^54p^2$	$R^1(4s^2, 4p^2)$	4.05	4.09
Co	0.042	−0.859	$4s3d^6$	$R^2(4s3d, 3d^2)$	−0.55	−0.32
	3.814	2.701	$3d^7$	$R^2(4s^2, 3d^2)$	1.51	1.36
	22.120	26.160	$3d^34s^24p^2$	$R^1(3d^2, 4p^2)$	0.99	0.89
				$R^3(3d^2, 4p^2)$	0.79	0.72
	7.985	7.843	$3d^54p^2$	$R^1(4s^2, 4p^2)$	4.36	4.38

is no SCK decay and the line widths are typically one order of magnitude smaller. Hence, resonances overlap very weakly and the 2p photoabsorption spectra can be described using the Fano theory.

For photoemission spectra, on the other hand, electron correlations are very important even in the energy region of 2p excitations as we will show in the following section.

5. Photoelectron spectroscopy of free 3d metal atoms

The first experiments on direct photoemission (photoelectron spectroscopy with excitation well above the ionization threshold) in the core level regions of free 3d metal atoms were performed by the group of Schmidt on Mn 3p [190] and by the groups of Fadley, Gerard and Manson on Mn 3s and 3p [191, 192]. These pioneering investigations were followed by results on direct 3p photoemission of Mn and Cr [34, 193], Fe [194, 195], Ni [196], Sc [197] and Co [195].

2p photoelectron spectra of free 3d transition metal atoms with analyses based on HF calculations were reported for Cr [32, 31], Mn [198], Ni [37], Sc [185], Co and Cu [199] and Fe [38]. Bagus and co-workers presented an alternative theoretical approach based on Dirac–Fock calculations [200].

5.1. Direct 3p photoemission of 3d metal atoms

In figures 13 and 14 the experimental and corresponding calculated 3p photoemission spectra are shown. All spectra were taken with photon energies at least 50 eV above the ionization thresholds. For all measured spectra except for Cu the line width is limited by the experimental resolution.

The 3p photoelectron spectra are dominated by the Coulomb exchange interaction between the 3p hole and the 3d electrons. This typically spreads the spectra over an energy range of

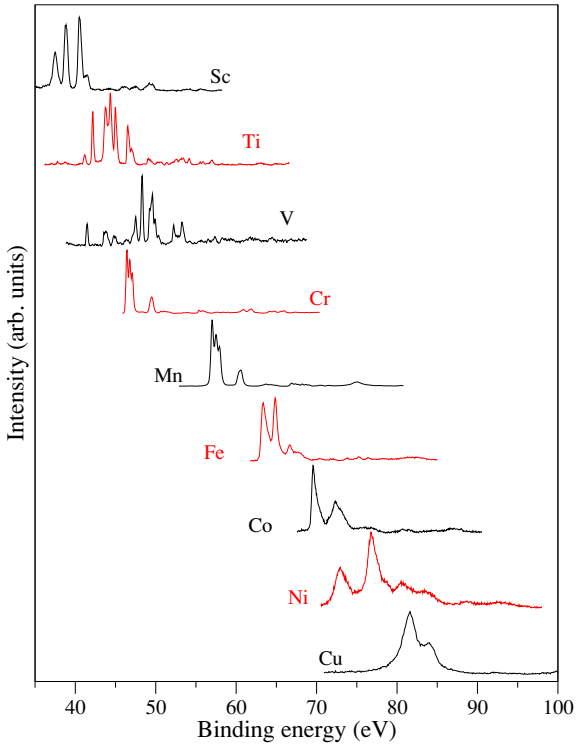

Figure 13. Overview of experimental 3p photoelectron spectra of free 3d metal atoms. Data are taken from the following references: Sc [197], Ti, V [175], Cr, Mn [193], Fe, Co [195], Ni [196] and Cu [137].

up to 20 eV and separates the so-called high- and low-spin states (where the resulting spin of the 3p core shell and of the 3d shell are parallel and anti-parallel, respectively). The situation is different only for Cu where the 3d subshell is closed and no 3p–3d exchange interaction occurs. The spectrum hence reflects two spin–orbit split lines, see figure 13.

It is apparent from figures 13 and 14 that Cr plays a special role in the series of the 3p photoelectron spectra of the 3d metal atoms: the binding energies of the high-spin main lines are distinctly smaller compared to the neighbouring 3d elements, V and Mn. For the $3p^5 3d^5 4s$ configuration the wavefunctions are located at larger radii as compared to the $3p^5 3d^4 4s^2$ configuration. By increasing the number of electrons in the 3d subshell, the Coulomb repulsion of the 3d electrons becomes larger increasing the centre of gravity $\langle r_{3d} \rangle$ of the 3d electron density. Also the 4s wavefunction extends to larger radii, because the core charge is better screened in the $3d^5$ configuration by the additional 3d electron. This results in a smaller binding energy of the $3p^5 3d^5 4s$ configuration compared to the $3p^5 3d^4 4s^2$ configuration.

We use the Mn 3p photoelectron spectrum in figure 15 as a prototypical example to introduce the major interactions and effects involved. Mn has the advantage that only the $3d^5 4s^2\ {}^6S_{5/2}$ ground state has to be taken into account to describe the experimental spectrum, because no thermal population of other initial states occurs at the experimental evaporation temperature. Furthermore, coupling with the closed 4s shell can be neglected.

The dominating 3p–3d Coulomb interaction separates the ^7P (high-spin) and ^5P (low-spin) states in Mn by about 18 eV. The spin–orbit splitting in the 3p shell gives rise to an

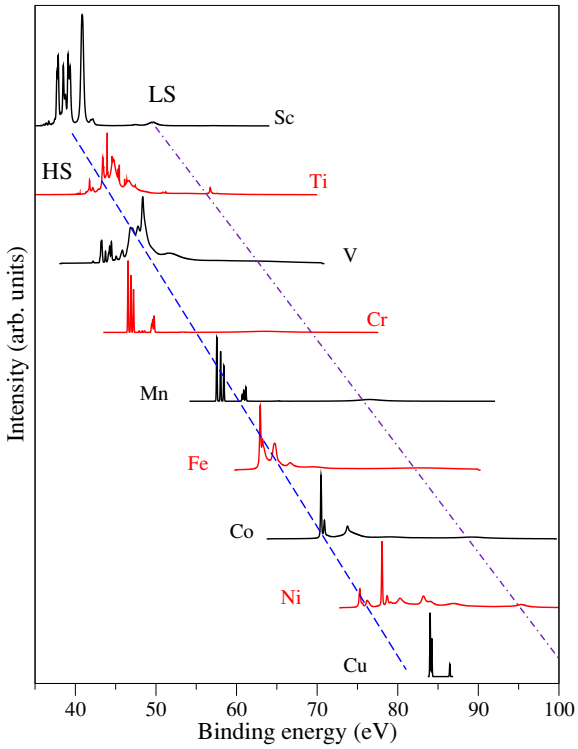

Figure 14. Overview of theoretical 3p photoelectron spectra of free 3d metal atoms. SCA calculations have been applied for Cr, Mn [141], Fe, Co [195], Ni [196], while for Sc [197] and Ti, V, Cu [141] CI calculations were used. For Sc, Ti, V, Fe, Co and Ni the thermal population of different initial states had to be taken into account additionally. The spectra have been convoluted with a 0.1 eV Gaussian to more clearly recognize sharp features in the spectra. Other than that line widths directly correspond to calculated line widths. The dashed and dashed-dotted lines approximately mark energies of the high-spin (HS) and low-spin (LS) states, respectively.

additional fine structure ($^7P_4$, $^7P_3$, $^7P_2$) which is clearly resolved in the Mn high-spin main lines in figure 15. Since this spin–orbit splitting (<1 eV) is much smaller than the splitting caused by the 3p–3d Coulomb interaction, *LS*-coupling serves as a good approximation of the final states. Recoupling of the 3d shell (spin flips) and shake-up processes (4s to 4p transitions, for example) further complicate the spectra and corresponding satellite lines are visible in the spectrum. In the ground state the $3d^5$ configuration couples to ^6S, where all 3d spins are parallel (Hund's rule). By recoupling the 3d electrons with one or two flipped 3d spins ^4L or ^2L states are obtained. The satellite lines that are separated by about 4 eV from the high-spin main lines (figure 15) correspond to a recoupled 3d shell with one 3d spin flip. The small features at 64 eV binding energy can be assigned to final states with a recoupled 3d shell with two 3d spin flip. The group of lines at 67 eV and 68 eV binding energy are due to 4s to 5s and 4s to 4d shake-up transitions.

The interpretation of the 3p photoelectron spectra was a puzzle for some time because the measured spectra did not display the high- and low-spin components with the expected intensities corresponding to their multiplicities (intensity ratio of 15:11 for the ^7P:^5P high:low spin components of Mn 3p for example, see figure 15). It was realized very early on by McGuire [201], Kotani [17], Ogasawara *et al* [202], Okada *et al* [203], Malutzki [190] and

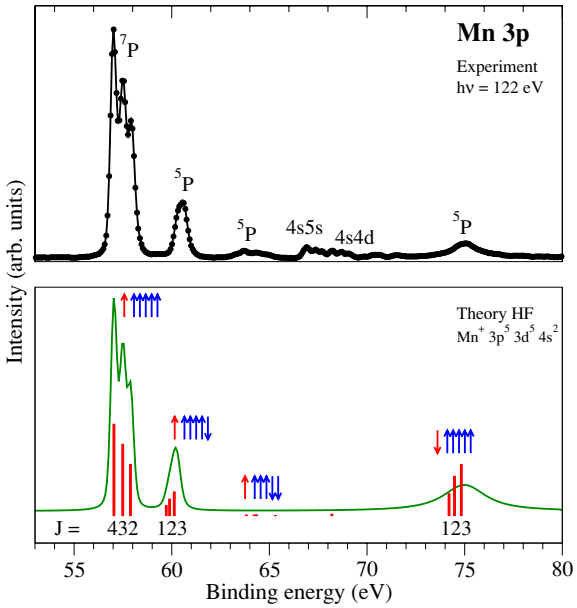

Figure 15. Comparison of the experimental (top panel) and calculated (bottom panel) Mn 3p photoelectron spectra. All spectra are taken from [193]. The spins of the 3p and 3d electrons are sketched by arrows. The bars in the calculated spectrum (bottom panel) correspond to the oscillator strengths calculated within the SCA and reflect the multiplicity of the states. The calculated spectrum shown as the solid line (bottom panel) includes the strongly term-dependent line widths as calculated with CI [193]. This shows that the spin-dependent core hole decay substantially broadens and suppresses the ^{5}P low-spin lines.

Schmidt [204] that a spin dependence of the Auger decay rates of the 3p hole is essential for the description of the 3d metal 3p photoelectron spectra. As a result of this spin dependence the low-spin states are substantially broadened and suppressed in the spectra (see the case of Mn in figure 15). Von dem Borne *et al* presented a detailed analysis of the Mn and Cr 3p photoelectron spectra based on calculations by Hansen [193]. Later, similar analyses were reported for Fe and Co [195], Ni [196] and Sc [197]. Note that for Cu the SCK decay is possible for all states due to the closed 3d subshell resulting in a substantial broadening of the photoelectron lines (figure 13).

The finding about the forbidden SCK decay is sketched schematically in figure 16 for the case of Mn. The $3p^5$ configuration has a resulting $\uparrow$ spin and the resulting spin of the $3d^5$ configuration can couple either parallel or anti-parallel to the $3p^5$ spin. For the $3d^5$ configuration only the ground state with maximum spin is taken into account (Hund's rule). To fill the $3p\downarrow$ hole in the high-spin case a spin flip of one of the $3d\uparrow$ electrons would be required. This is strictly forbidden in the Coulomb interaction describing the Auger process. For the low-spin states the spin of the 3p hole and the 3d electrons match and the SCK process is allowed. This mechanism more generally results in a substantial line broadening for the low-spin states for all 3d elements from Sc to Ni as shown in table 8.

The line widths of the 3p photolines in table 8 have been calculated in a SCA and a CI approximation. For both calculations the line widths of the high-spin states are typically in the order of a few meV while the low-spin states have widths of up to several eV. The CI calculations include mixing of the $3d^n4s^2$, $3d^{n+1}4s$ and $3d^{n+2}$ configurations in the ground and in the final states for all elements. The line widths of both the low- and high-spin states

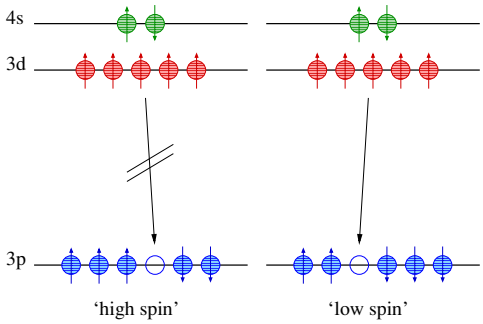

Figure 16. Decay of the high-spin and low-spin states of a Mn 3p core hole. For the high-spin states the 3d $\uparrow \rightarrow$ 3p $\downarrow$ decay is spin forbidden. The low-spin states decay via a fast SCK decay. This entails a substantial broadening and a corresponding suppression of the low-spin states in the 3p photoelectron spectra.

Table 8. Typical average values for the calculated line widths of the high- and low-spin states of the 3p hole states of the 3d electrons in a SCA and a CI (FISCI) calculation. All line widths are given in units of eV.

	High spin		Low spin	
	SCA	CI	SCA	CI
Sc	3×10^{-3}	4×10^{-2}	0.2	0.9
Ti	1×10^{-3}	0.2	0.3	3
V	4×10^{-3}	0.2	1	7
Cr	2×10^{-5}	3×10^{-5}	5	10
Mn	3×10^{-3}	6×10^{-2}	3	11
Fe	7×10^{-3}	0.1	5	10
Co	5×10^{-2}	0.1	5	10
Ni	0.2	0.2	3	6

increase, when CI in the final ionic state (FISCI) is included in the calculations. The line widths of the high-spin states increase by up to two orders of magnitude because already a small admixture of low-spin state character opens the SCK decay channel. This shows the strong influence of correlations on the lifetime of the 3p core hole states. The effect is smaller for the low-spin states and amounts to a factor of 2 for the elements from Cr to Ni and up to a factor of 10 for Ti and V. For Mn Hansen has performed a more refined CI calculation further including the interaction with the 4d and 3s electrons [193], leading to a slightly increased line width of the main photolines.

For Cr the line width of the high-spin states is two orders of magnitude smaller than for the other elements. This is due to that for Cr the 4s $\rightarrow$ 3p decay is spin forbidden (the 4s spin is parallel to the 3d spins due to Hund's rule). Auger decay of the high-spin core hole of Cr is only possible by small admixtures of low-spin character to the high-spin wavefunctions due to the spin–orbit interaction.

The high-spin line width increases from Cr to Ni, as can also be seen in figure 13. Due to the subsequent filling of the 3d subshell SCK channels open up also for the high-spin states. The line width of the low-spin states increases from Sc to Cr due to the increasing numbers of possible SCK channels. The low-spin line width of Sc is comparably small because the 3d shell is occupied by only one electron and, therefore, no SCK but only a Coster–Kronig (CK) decay can occur.

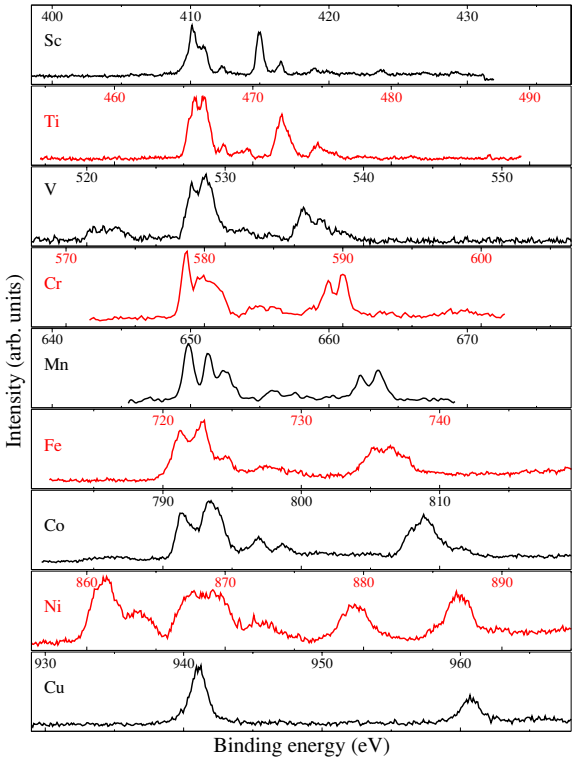

Figure 17. Overview of the experimental 2p photoelectron spectra of the 3d metal atoms. Data are taken from the following references: Sc [185], Ti, V [175], Cr [32, 31], Mn [198], Fe [38], Co [199], Ni [37] and Cu [199].

The broadening of the low-spin states has already been studied theoretically in the condensed phase for several 3d transition metal compounds by Kotani and co-workers [17, 205, 187]. However, in these calculations the decay of the high-spin states has not been taken into account, because in solids the lifetime of these states is strongly influenced by the interaction of one atom with the surrounding ligands. This can be understood as a generalized CI resulting in a larger line width as compared to the free atoms.

5.2. Direct 2p photoemission of 3d metal atoms

Figure 17 depicts an overview of the measured 2p photoelectron spectra for all 3d elements. All spectra were taken at photon energies around 50–100 eV above the ionization thresholds. The corresponding theoretical spectra are shown in figure 18. In a simple one-electron picture, often used for the interpretation of the 2p photoelectron spectra of bulk metals, only two lines corresponding to the spin–orbit split $2p^{-1}_{1/2}$ and $2p^{-1}_{3/2}$ core hole states should be observed. For the free atom this is only the case for Cu: due to the closed 3d shell no additional multiplet splitting occurs. The spectra of all other elements are more complex due to the influence of the 2p–3d core–valence Coulomb interaction, the recoupling of the 3d shell, and due to photoemission from thermally excited ground states.

As for 3p photoemission presented above, we use Mn to discuss some fundamental interactions affecting the 2p photoelectron spectra of free 3d metal atoms. Figure 19 depicts

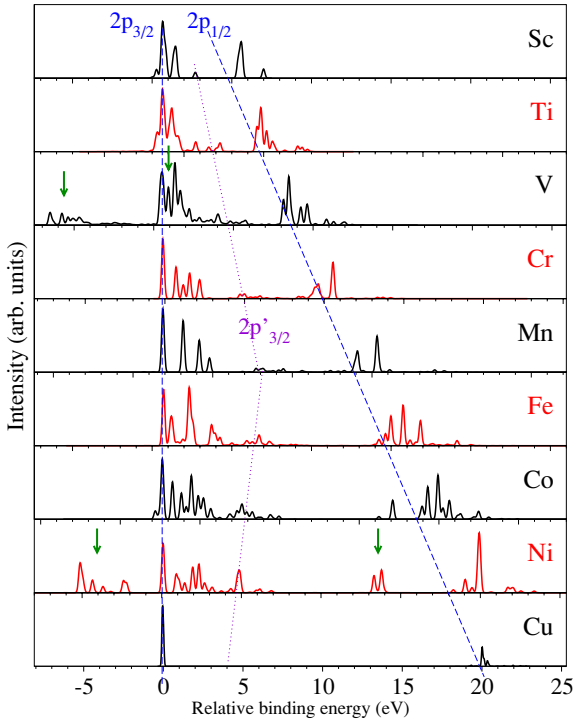

Figure 18. Overview of the calculated 2p photoelectron spectra of the 3d metal atoms on a relative binding energy scale. Zero binding energy is set for each spectrum to the energy of the line with lowest binding energy in the $2p_{3/2}^{-1}$ multiplet. The dashed line indicates the evolution of the binding energies of the $2p_{1/2}^{-1}$ multiplets. This shows the increasing spin–orbit splitting with increasing nuclear charge Z. The dotted line indicates the evolution of the binding energies of 3d-recoupled satellite lines. All spectra have been convoluted arbitrarily with a 200 meV Gaussian. The arrows in the V and Ni spectra indicate the additional lines due to the excitations from thermally populated $3d^n4s$ configurations (see the text). Calculations taken from: Sc [185], Ti, V [141], and Cr–Cu [199].

the measured (top panel) and calculated (middle and bottom panel) 2p photoelectron spectra of free Mn atoms [198].

Already the single configuration approximation (SCA) calculation describes the experimental data very well. Therefore electron–electron correlations, which might be described in a CI approach, can be assumed to be small and in the following the influence of the $4s^2$ electrons is neglected.

Due to the dominating spin–orbit interaction of the 2p shell the two groups of lines at 650 and 665 eV can be assigned to spin–orbit split $2p_{3/2}^{-1}$ and $2p_{1/2}^{-1}$ core hole states. Additional multiplet splitting due to the Coulomb interaction of the 2p core hole and the $3d^5$ valence shell causes the resolved fine structure that spreads the lines in each group over about 4 eV. Coupling of the total angular momentum of the core hole $j = 3/2, 1/2$ to the total spin of the 3d valence electrons $S = 5/2$ yields the total angular momenta J of the four (two) final states in the $2p_{3/2}^{-1}$ $\left(2p_{1/2}^{-1}\right)$ multiplets. This corresponds to the jK-coupling scheme [206, 31].

As for 3p photoemission, recoupling of the 3d valence shell gives rise to the satellite lines at about 4 eV higher binding energy compared to the main lines (see the arrows depicted in panel (b) of figure 19). In figure 19(c) the contributions from the different $3d^5\ ^{6,4,2}L$ multiplet

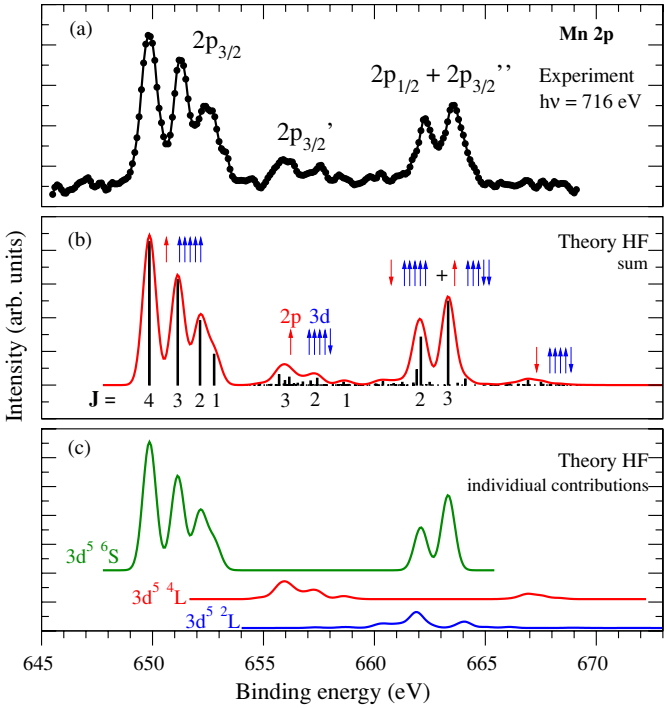

Figure 19. (a) Experimental and (b) theoretical 2p photoelectron spectra of atomic Mn. The spin of the 2p and 3d electrons is sketched in panel (b). Panel (c) depicts the calculated individual contributions to the sum shown in (b) from the different $3d^5\ ^{2S+1}L$ multiplet terms separately. The calculated spectra have been convoluted with a 0.7 eV Gaussian to take into account the experimental broadening. A more detailed discussion can be found in [198, 206].

terms are shown separately. The satellite between the main lines at binding energies around 656 eV, denoted as $2p'_{3/2}$, can therefore be assigned to low-spin states with a $2p^{-1}_{3/2}$ core hole and a recoupled valence shell with one spin flipped 3d electron. The $2p^{-1}_{3/2}3d^5(^2L)$ satellites with two flipped 3d spins, denoted as $2p''_{3/2}$ in figure 19, are shifted up in energy by another 6 eV. As a consequence, they have almost the same binding energy as the $2p^{-1}_{1/2}3d^5(^6\mathrm{S})$ main lines which causes mixing of these states.

This mixing could be directly visualized for Cr 2p photoemission, where the situation is very similar, by measuring the dichroism in the 2p photoelectron spectra of laser-aligned free Cr atoms [31, 206]. Thus, the simple one-electron picture to describe the 2p photoelectron spectra with spin–orbit split pure $2p^{-1}_{3/2}$ and $2p^{-1}_{1/2}$ states, often used in solid state physics, is not valid: the $2p^{-1}_{1/2}$-like states also have appreciable amounts of $2p^{-1}_{3/2}$ character [198]. In a more general sense, the dichroism in the 2p photoelectron spectra of laser-oriented free Cr atoms can help understand the electronic structure of thin magnetized Cr films [32].

The $2p^{-1}_{1/2}\ 3d^5\ ^2L$ states have almost no intensity and while they could not be observed for Mn 2p they are clearly apparent in the Cr 2p photoelectron spectra [32, 198, 31].

The $2p'_{3/2}$ low-spin satellites can be observed in all 2p photoelectron spectra from Ti to Ni. In figure 18 their binding energies are marked with a dotted line. The splitting Δ' between the $2p'_{3/2}$ satellite and $2p^{-1}_{3/2}$ main line is increasing from Ti to Mn and is then decreasing up to Ni. This behaviour can be qualitatively understood from the properties of anti-symmetric

wavefunctions and it is a result of the spin-dependent Coulomb exchange interaction described in section 2.1. According to Hund's rule, for a less than half-filled $3d^n$ configuration ($n \leqslant 5$) in the ground state the spin of the 3d subshell will be maximized. This is a result of the smaller Coulomb repulsion energy, because for parallel (symmetric) spins the spatial wavefunction $\Psi(\vec{r})$ has to be anti-symmetric (Pauli principle). Hence, the probability to find two 3d electrons at the same spatial position $\vec{r}$ is zero, minimizing the Coulomb repulsion. If now the spin of one 3d↑ electron is changed, the spatial wavefunction $\Psi(\vec{r})$ is symmetric and two 3d electrons with different spin might occupy the same spatial orbital. With an increasing number of $(n-1)$ 3d↑ electrons, the probability for a 3d↓ electron to occupy the same spatial orbital $\Psi(\vec{r})$ as any of the $(n-1)$ 3d↑ increases linearly with $(n-1)$. Thus the Coulomb repulsion and the splitting Δ' increases with the number n of 3d electrons, in agreement with experiment. The largest splitting Δ' is observed for Cr and Mn with a $3d^5$ configuration. For this configuration, the largest Coulomb repulsion proportional to $n-1=4$ is obtained.

The situation is similar for a more than half-filled $3d^n$ subshell. Changing the spin of a 3d↑ electron results in the maximum Coulomb repulsion, as for Cr and Mn. However, for $n \geqslant 6$ there are already filled 3d↓ orbitals. Thus, the Coulomb repulsion with the remaining four 3d↑ electrons increases, but the repulsion with the $(n-5)$ 3d↓ electrons decreases. Thus, the $\Delta' \propto 4-(n-5)=(9-n)$ is decreasing with the number n of 3d electrons.

Furthermore, also the energy splitting Δ'' between the $2p''_{3/2}$ satellites and the $2p^{-1}_{3/2}$ main line can be explained using this model. Here the spins of two 3d electrons are changed leading to almost twice the shift $\Delta' = \Delta_{\uparrow\rightarrow\downarrow}$ for the $2p''_{3/2}$ satellites (see figure 19).

For V and Ni three and four groups of lines are observed, respectively. In figure 18 the additional groups are marked with arrows. As mentioned before in section 3 for these atoms the excitation in an atomic beam at the relatively high evaporation temperatures occurs from two different thermally populated initial state configurations, namely $3d^k4s^2$ and $3d^{k+1}4s$ with $k=8, k=3$ for Ni and V respectively. With near degenerate initial configurations and the $\simeq$8 eV splitting of the corresponding core hole configurations four groups of lines appear. However, for V the $2p^{-1}_{1/2}3d^44s$ and $2p^{-1}_{3/2}3d^34s^2$ groups have almost the same binding energy of $\simeq$ 526–528 eV and therefore only three of the 2p core hole groups of lines are observed. The energetic ordering of the configurations is reversed by the 2p hole, whereas energetic ordering is conserved in cases where the 2p core electron is not fully removed but present as an additional valence electron such as in 2p photoabsorption [18]. This explains the appearance of the second doublets shifted towards lower binding energies here, while there was no sign of them in figure 10 (2p photoabsorption).

Sc has only one 3d electron, therefore no low-spin satellite is observed. The small satellites in the Sc 2p photoelectron spectrum at 3 eV and 7 eV above the main $2p^{-1}_{3/2}$ line in figure 18 can be assigned to $2p^{-1}_{3/2}4s^23d\ ^3D_1$, and $2p^{-1}_{1/2}4s^23d\ ^1P_1$ states. The large splitting of 7 eV observed for the $^1P_1$ state is attributed to the unusually large g_1 angular coefficient of the G^1 Slater integral.

This is similar to the Sc 3p photoemission discussed in [197]. However, for 2p photoemission the situation is more complicated, because the spin–orbit splitting $\zeta_{2p} = 3.0$ eV and the Slater integral $G^1(2p, 3d) = 2.7$ eV are of comparable size. Hence, the electronic structure has to be described in intermediate coupling. Nevertheless, the interpretation based on the 3p photoelectron spectrum can partly be used for 2p photoemission as well. Here also the $^3D_1$ state shows a relatively large splitting due to a large admixture of $^1P_1$ states in the order of 39%.

While the Cr and Mn 2p photoelectron spectra can be very well described by a SCA calculation, this model fails for the angular distribution parameter β. Only by using CI expansions to account for correlation effects is one able to obtain a good agreement with

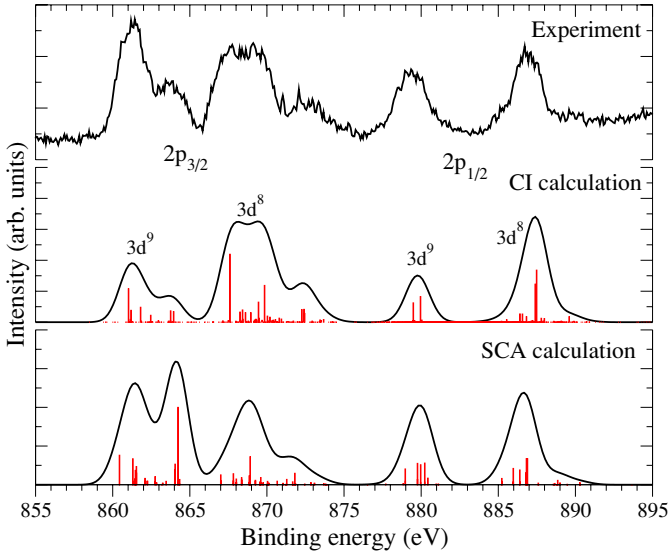

Figure 20. Experimental 2p photoelectron spectrum of atomic Ni (upper panel) in comparison with a theoretical SCA and CI model. The CI calculation includes the 3d–4s and 3d–4p valence interactions. The theoretical spectra have been convoluted with a 1.7 eV Gaussian to take into account the experimental broadening. Experimental spectrum and CI calculation taken from [37], SCA calculation from [141]. Theoretical spectra were energy shifted to match those of the experiment.

the measured angular distributions. The shape of the angle-independent (magic-angle) photoelectron spectrum, however, remains unaffected when changing from a SCA to a CI model [30].

The situation changes for Ni, where a mixing of several configurations has always to be taken into account. It has been shown that the 2p photoelectron spectrum of free Ni atoms can serve to understand the electronic structure of Ni in the condensed phase [37]. There, Ni is often referred to as a highly correlated system [186, 207, 188] because already for the description of the ground state a mixture of the $3d^8$, $3d^9$ and $3d^{10}$ configurations is necessary. In metallic Ni this is attributed to the narrow band character of the 3d band, equivalent to a stronger localization of the 3d electrons.

In figure 20 the 2p photoelectron spectrum of atomic Ni is shown in comparison to a SCA and a CI calculation. For both calculations, the Coulomb Slater integrals were scaled to 80% of their *ab initio* values. Both $2p^53d^84s^2$ line groups each show a satellite structure at lower binding energies (about 8 eV). These satellites can be assigned to the $2p^53d^94s$ configuration [37], due to the thermal population of $3d^94s$ in the ground state. The CI calculation includes the FISCI of the configurations $2p^53d^84s^2$, $2p^53d^94s$, $2p^53d^84p^2$ and $2p^53d^{10}$. In contrast to the simple SCA model, it reproduces all line groups very nicely. This shows a clear influence of electron–electron correlations already in the free Ni atom. However, in the CI model the intensities for the $2p^53d^94s$ photoemission lines are underestimated. At a first glance this could result from an incorrect assumption for the (thermal) population of the initial states. But this can be clearly ruled out: an increase in evaporation temperature of 1000 K has a 1% effect on the $3d^9/3d^8$ ratio only, because of the particular energetic ordering of the Ni ground state terms.

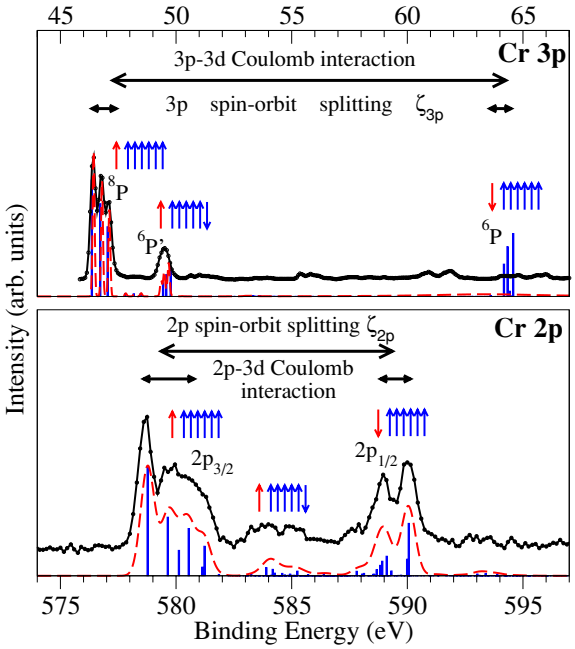

Figure 21. 3p (top, [193]) and 2p (bottom, [31]) photoelectron spectra of atomic Cr. Horizontal arrows indicate the energy splittings caused by the main interactions, which are the core-hole–3d valence Coulomb exchange interaction and the spin–orbit splitting of the core hole. Vertical arrows indicate the resulting spins of the 2p and 3p electrons (the 4s electrons are not considered).

High-resolution 2p photoemission experiments with a better resolved fine structure are highly desirable in particular for Ni. In principle this is possible, because the total line width of all presented experimental 2p photoelectron spectra is limited by the experimental resolution. The typical experimental resolution was in the order of 0.6–0.7 eV for Cr and Mn and 1.5–1.8 eV for the spectra of the other elements. The natural line width of the 2p lines is of the order of a few 100 meV. There are about ten channels $n_1\ell_1^{-1}n_2\ell_2^{-1}$, with $n\ell = 3s, 3p, 3d, 4s$ available for the decay of a 2p core hole in a 3d metal atom. However, in contrast to the 3p photoelectron spectrum no term-dependent lifetime broadening is observed for the 2p photolines since SCK decay is not possible and hence the line widths of low- and high-spin states are similar.

5.3. 3p and 2p photoemission in comparison

In a single configuration approximation, the 3p and 2p photoelectron spectra should display the same number of final states, but the coupling is quite different. In figure 21 the 3p and 2p photoelectron spectra of atomic Cr are compared to emphasize common features and differences. In both spectra, the photoelectron lines are spread in energy over 15–20 eV.

In the 2p photoelectron spectrum the main splitting is due to the 2p spin–orbit interaction which is a one-electron interaction (for Cr the 2p spin–orbit parameter amounts to $\zeta_{2p} \approx 6$ eV and the corresponding splitting is $3/2\zeta_{2p} \approx 9$ eV [206, 39]). The fine structure in each of the spin–orbit split groups of lines is due to the 2p–3d Coulomb exchange interaction which is of the order of a few eV (the splitting approximately corresponds directly to the values of the respective parameters $F^2(2p, 3d) = 4.9$ eV, $G^1(2p, 3d) = 3.5$ eV, $G^3(2p, 3d) = 2$ eV for Cr 2p ionization). The final states can be well described in jK-coupling [206, 31]. Finally, due

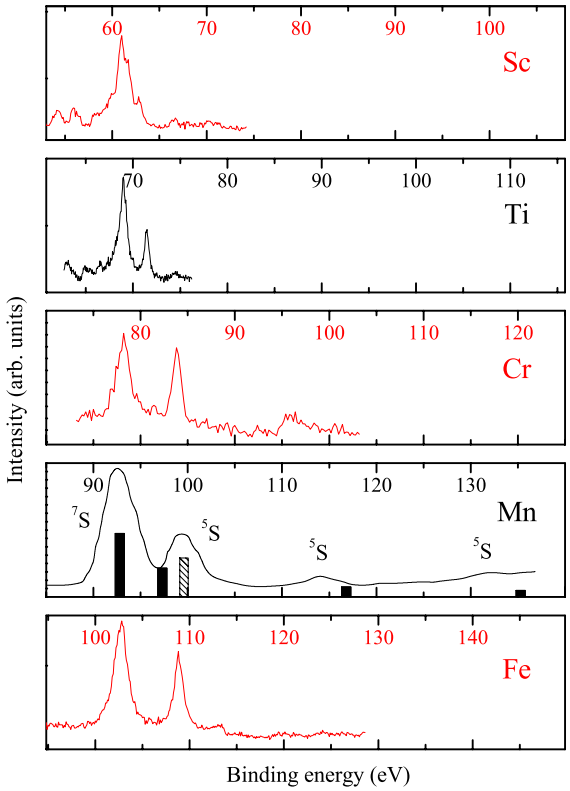

Figure 22. 3s photoemission spectra of Sc, Ti, Cr, Mn and Fe. (Data taken from the following references: Cr [193], Mn experiment [209], Mn calculations [210], Sc [137], Ti [136] and Fe [211].)

to 3d valence shell recoupling, additional 2p′ low-spin satellites occur at about 4 eV higher binding energies compared to the main lines.

The respective roles of the main interactions in the 3p photoelectron spectra are opposed to the 2p case. The main splitting between the high-spin ^{8}P and low-spin ^{6}P lines is due to the two-particle 3p–3d Coulomb exchange interaction which is of the order of about 17 eV ($G^1(3p, 3d) = 14.3$ eV, and $G^3(3p, 3d) = 8.6$ eV [208]). The 3p spin–orbit parameter amounts to $\zeta_{3p} \approx 0.7$ eV, which is one order of magnitude smaller than the Coulomb interaction and hence, it only contributes to the fine structure of the lines. The 3p photoelectron spectrum can therefore be well described based on LS-coupling. Note that the spin–orbit fine structure is not visible in the ^{6}P low-spin state due to the large lifetime broadening. The ^{6}P′ satellite with a shift of ≈4 eV with respect to the high-spin ^{8}P line, can be described as a 3d recoupling satellite equivalent to the 2p′ satellite in the 2p excitation. The 3d spin–orbit parameter is of the order of $\zeta_{3d} \approx 0.05$ eV and does not need to be taken into account in the analysis of both the 3p and 2p photoelectron spectra.

Probably the largest and most obvious difference between the 2p and 3p photoelectron spectra is the strong lifetime broadening of the 3p low-spin states due to the (3d → 3p, 3d → $\epsilon\ell$) SCK decay. The 2p core hole has many more decay channels. However, even when summing over all these decay channels, the 3p SCK is still much faster, due to the larger overlap of the 3p with the 3d wavefunctions.

5.4. The 3s excitation

Figure 22 depicts a selection of 3s photoelectron spectra of 3d metal atoms. To our knowledge, to date no further experimental spectra have been reported and theoretical calculations exist only for Mn.

The Mn 3s photoemission has drawn considerable attention in the past and we use it here to discuss the main features of the 3d metal 3s photoelectron spectra. The ground state electron configuration of Mn is $3s^2 3p^6 3d^5 4s^2$. The 4s electrons do not influence the coupling and can be omitted from the term labels together with the closed inner shells. The half-filled 3d shell, $3d^5$, couples to ^{6}S and lies much lower in energy than all other states of the $3d^5$ configuration (Hund's rule). Removing a 3s electron leads to $3s3p^6(3d^5\ ^6S)\ ^7S$ or ^5S terms as long as the coupling in the 3d shell is unchanged. Thus two photoelectron peaks are expected, separated by a distance determined by the exchange interaction between the 3s and 3d electrons. The 3s and 3d orbitals are located in the same region of space and the exchange interaction between them is consequently considerable. Hence, the distance between the ^{7}S and ^{5}S peaks is expected to be large. The relative intensity of the peaks is, within the approximations, determined by the statistical degeneracy of the two terms, i.e., $7/5 = 1.4$. However, the energy separation and the relative strengths of the corresponding lines in the photoelectron spectra of both atoms and solids [191, 192, 212] strongly deviate from these predictions. In addition, further peaks were observed in the spectra which originally were ascribed to solid state screening but later were realized to be due to intra-atomic interactions [191]. The 3s spectrum has therefore a rather prominent place in the history of the use of atomic concepts in the interpretation of solid state spectra. By taking into account strong intra-atomic CI the theoretical spectra could be adjusted to the experimental results [212, 213]. CI with $3s^2 3p^4 3d^6$ moves the $3s3p^6(3d^5\ ^6S)\ ^5S$ term closer to $3s3p^6(3d^5\ ^6S)\ ^7S$, which is much less perturbed. Configuration interaction distributes the $3s3p^6(3d^5\ ^6S)\ ^5S$ intensity over several ^{5}S states thus increasing the intensity ratio $3s3p^6(3d^5\ ^6S)\ ^7S/3s3p^6(3d^5\ ^6S)\ ^5S$ from 1.4 to more than 2 (black bars in figure 22). Recently, Bagus *et al* [210] have expanded their CI calculations to include interaction with the 4f orbital (hatched bar in figure 22). This inclusion increases the ^{7}S–^{5}S energy splitting by about 2 eV and, as compared to the previous calculation, this results in a much better agreement with the experiment.

6. Summary

This review summarizes results on the core level photoionization of the free 3d transition metal atoms. The influence of multi-electron interactions in these open shell atoms and the interpretation of the experimental photoabsorption and photoemission data by *ab initio* calculations based on HF and CI models are discussed. Comparison of the spectra of all 3d transition metal atoms emphasizes common features and distinct differences. The fundamental effects and main interactions which determine the electronic structure of these elements become apparent. The knowledge of the electronic structure of the free atoms is of importance in order to disentangle intra- and inter-atomic effects in the core level spectra of 3d metal thin films and compounds.

The major findings are as follows. The 3p photoabsorption shows a different behaviour for the early and the late 3d transition metal atoms. Mn and the late transition metals Fe, Co and Ni can be well described in terms of a single configuration approximation, when the shift of the $3p \rightarrow 3d$ resonance position due to the interaction with the continuum states is taken into account. The early 3d elements Sc, Ti and V have to be described in a configuration interaction approach.

In contrast to 3p the 2p photoabsorption can be described in a single configuration approximation for all 3d elements from Sc to Ni. Only for Sc is a small influence of the 4d Rydberg orbitals observed. This is a result of the much larger 2p spin–orbit splitting as compared to 3p and the missing SCK decay channel in the 2p photoionization. Therefore the 2p excited states are spread over a larger energy range, which results in a much smaller CI of the core hole excited states.

The 3p photoelectron spectra are dominated by the large 3p–3d Coulomb exchange splitting and the term-dependent decay of the 3p core hole states. The Coulomb exchange interaction results in a splitting of high- and low-spin states of around 20 eV. For the high-spin states the super-Coster–Kronig decay 3d $\rightarrow$ 3p, 3p $\rightarrow \epsilon\ell$ is forbidden, resulting in a line width of up to several orders of magnitude smaller than that of the low-spin states. This affects the 3p photoelectron spectra of all 3d elements from Ti to Ni and results in the prominent suppression of the low-spin states in the 3p spectra. The influence of electron correlations on the 3p photoemission is similar to their influence on the 3p photoabsorption process. The energy positions of the photolines of the late transition metals, including Cr and Mn, can well be described within a single configuration approximation, whereas for the early elements Sc, Ti and V a configuration interaction (CI) approach has to be used.

The 2p photoelectron spectra of most 3d transitions metals are well described within a single configuration approximation. The 2p spin–orbit splitting dominates the spectra. Core–valence 2p–3d Coulomb interactions and recoupling of the 3d valence shell (spin flips) further complicate the spectra and lead to a rich fine structure. As a consequence, the one-electron model, which is often used for the 2p excitations in 3d metal thin films and solids, is not particularly suitable to explain the experimentally observed features.

Acknowledgments

For discussions and advice on particular points the authors would like to thank Andreas von dem Borne, John Costello, Robert D Cowan, Christopher Gerth, Alexei N Grum-Grzhimailo, Jørgen Hansen, Nikolai Kabachnik, Bernd Sonntag, Kai Tiedtke, Andreas Verweyen and Scott Whitfield.

References

[1] Grünberg P, Schreiber R, Pang Y, Brodsky M B and Sowers H 1986 Layered magnetic structures: evidence for antiferromagnetic coupling of Fe layers across Cr interlayers *Phys. Rev. Lett.* **57** 2442

[2] Baibich M N, Broto J M, Fert A, Nguyen Van Dau F, Petroff F, Eitenne P, Creuzet G, Friederich A and Chazelas J 1988 Giant magnetoresistance of (001)Fe/(001)Cr magnetic superlattices *Phys. Rev. Lett.* **61** 2472

[3] Camley R E and Barnas J 1989 Theory of giant magnetoresistance effects in magnetic layered structures with antiferromagnetic coupling *Phys. Rev. Lett.* **63** 664

[4] Binasch G, Grünberg P, Saurenbach F and Zinn W 1989 Enhanced magnetoresistance in layered magnetic structures with antiferromagnetic interlayer exchange *Phys. Rev.* B **39** 4828

[5] Kusters R M, Singleton J, Keen D A, McGreevy R and Hayes W 1989 Magnetoresistance measurements on the magnetic semiconductor $Nd_{0.5}Pb_{0.5}MnO_3$ *Physica* B **155** 362–5

[6] von Helmolt R, Wecker J, Holzapfel B, Schultz L and Samwer K 1993 Giant negative magnetoresistance in perovskitelike $La_{2/3}Ba_{1/3}MnO_x$ ferromagnetic films *Phys. Rev. Lett.* **71** 2331–3

[7] Khomskii D I and Sawatzky G A 1997 Interplay between spin, charge and orbital degrees of freedom in magnetic oxides *Solid State Commun.* **102** 87

[8] Elfimov I S, Anisimov V I and Sawatzky G A 1999 Orbital ordering, Jahn–Teller distortion and anomalous x-ray scattering in manganates *Phys. Rev. Lett.* **82** 4264

[9] Castleton C W M and Altarelli M 2000 Orbital ordering in the manganites: resonant x-ray scattering predictions at the manganese L_{II} and L_{III} edges *Phys. Rev.* B **62** 1033

[10] Yoshizawa H, Kakeshita T, Kajimoto R, Tanabe T, Katsufuji T and Tokura Y 2000 Stripe order at low temperatures in $La_{2-x}Sr_xNiO_4$ with $0.289 \leqslant x \leqslant 0.5$ *Phys. Rev.* B **61** R854

[11] Goodenough J B 1963 *Magnetism and the Chemical Bond* (New York: Interscience)

[12] Kanomori J 1959 Superexchange interaction and symmetry properties of electron orbitals *J. Phys. Chem. Solids* **10** 87

[13] Mannella N, Rosenhahn A, Booth C H, Marchesini S, Mun B S, Yang S-H, Ibrahim K, Tomioka Y and Fadley C S 2004 Direct observation of high-temperature polaronic behavior in colossal magnetoresistive manganites *Phys. Rev. Lett.* **92** 166401

[14] Ebert H, Baumgarten L, Schneider C M and Kirschner J 1991 Polarization dependence of the 2p-core-hole photoemission spectra of Fe *Phys. Rev.* B **44** 4406–9

[15] Cherepkov N A 1994 Origin of magnetic dichroism in angular-resolved photoemission from ferromagnets *Phys. Rev.* B **50** 13813–6

[16] van der Laan G 1995 Angular-resolved linear and circular dichroism in core-level photoemission of metallic systems *Phys. Rev.* B **51** 240–9

[17] Taguchi M, Uozume T and Kotani A 1997 Theory of x-ray photoemission and x-ray emission spectra in Mn compounds *J. Phys. Soc. Japan.* **66** 247–56

[18] de Groot F M F 1994 X-ray absorption and dichroism of transition metals and their compounds *J. Electron Spectrosc. Relat. Phenom.* **67** 529–622

[19] de Groot F M F 2005 Multiplet effects in x-ray spectroscopy *Coord. Chem. Rev.* **249** 31–63

[20] Bruhn R, Schmidt E, Schröder H and Sonntag B 1982 VUV photoabsorption and photoemission of atomic Cr *J. Phys. B: At. Mol. Phys.* **15** 2807–17

[21] Bruhn R, Schmidt E, Schröder H and Sonntag B 1982 Resonant satellite photoemission of atomic Cu *J. Phys. B: At. Mol. Phys.* **15** L441–4

[22] Schmidt E, Schröder H, Sonntag B, Voss H and Wetzel H E 1983 Resonant vacuum ultraviolet photoemission of atomic Fe, Co and Ni *J. Phys. B: At. Mol. Phys.* **16** 2961–9

[23] Schmidt E, Schröder H, Sonntag B, Voss H and Wetzel H E 1984 $M_{2,3}$-shell Auger and autoionization spectra of free Cr, Mn, Fe, Co, Ni and Cu atoms *J. Phys. B: At. Mol. Phys.* **17** 707–18

[24] Krause M O, Carlson T A and Fahlman A 1984 Photoelectron spectrometry of manganese vapor between 12 and 110 eV *Phys. Rev.* A **30** 1316–24

[25] Garvin L J, Brown E R, Carter S L and Kelly H P 1983 Calculation of photoionisation cross sections, resonance structure and angular distribution for Mn I by many-body pertubation theory *J. Phys. B: At. Mol. Phys.* **16** L269–74

[26] Whitfield S B, Krause M O, van der Meulen P and Caldwell C D 1994 High-resolution photoelectron spectrometry of atomic manganese from the region of the 3p → 3d giant resonance to 120 eV *Phys. Rev.* A **50** 1269–86

[27] Verweyen A, Wernet Ph, Glatzel P, Sonntag B, Gerth Ch, Godehusen K and Zimmermann P 2000 Resonant 3p photoelectron spectroscopy of free Cu atoms *J. Phys. B: At. Mol. Opt. Phys.* **33** 1563–73

[28] Whitfield S B, Wehlitz R and Martins M 2004 Experimental and theoretical studies of metal vapor atoms *Rad. Phys. Chem.* **70** 3–42

[29] Whitfield S B, Caspary K, Myers T, Bjelland M, Wehlitz R, Jimenez-Mier J, Olalde-Velasco P and Krause M O 2005 Valence satellite photoionization of atomic scandium in the region of the 3p–3d giant resonance *J. Phys. B: At. Mol. Opt. Phys.* **38** 3273–87

[30] Godehusen K, Wernet Ph, Richter T, Zimmermann P and Martins M 2003 Multiplet resolved determination of the β-parameter for atomic Mn and Cr: a benchmark test for core-electron photoionization theories *Phys. Rev.* A **68** 052707

[31] Wernet Ph, Schulz J, Sonntag B, Godehusen K, Zimmermann P, Grum-Grzhimailo A N, Kabachnik N M and Martins M 2001 2p photoelectron and linear magnetic and alignment dichroism spectra of atomic Cr *Phys. Rev.* A **64** 042707

[32] Wernet Ph, Schulz J, Sonntag B, Godehusen K, Zimmermann P, Martins M, Bethke C and Hillebrecht F U 2000 Core–valance interaction in the linear dichroism of Cr 2p photoelectron spectra *Phys. Rev.* B **62** 14331–6

[33] Prümper G, Kröger S, Müller R, Martins M, Viefhaus J, Zimmermann P and Becker U 2003 Magnetic circular dichroism in the ion yield of polarized chromium atom at the 2p-edge *Phys. Rev.* A **68** 032710

[34] von dem Borne A, Dohrmann T, Verweyen A, Sonntag B, Godehusen K and Zimmermann P 1997 Dichroism in the 3p photoionization of polarized Cr atoms *Phys. Rev. Lett.* **78** 4019–21

[35] Dohrmann Th, von dem Borne A, Verweyen A, Sonntag B, Wedowski M, Godehusen K and Zimmermann P 1996 Linear dichroism in the core-resonant photoelectron spectra of laser-aligned Cr atoms *J. Phys. B: At. Mol. Opt. Phys.* **29** 5699–710

[36] von dem Borne A, Dohrmann Th, Verweyen A, Sonntag B, Godehusen K, Zimmermann P and Kabachnik N M 1998 Linear dichroism in photo-induced Auger electron emission from aligned Cr atoms *J. Phys. B: At. Mol. Opt. Phys.* **31** L41–8

[37] Godehusen K, Richter T, Zimmermann P and Martins M 2002 On the 2p photoionization of atomic Ni—a comparison with Ni metal and NiO photoionization *Phys. Rev. Lett.* **88** 217601

[38] Richter T, Godehusen K, Martins M, Wolff T and Zimmermann P 2004 Interplay of intra-atomic and interatomic effects: an investigation of the 2p core level spectra of atomic Fe and molecular $FeCl_2$ *Phys. Rev. Lett.* **93** 023002

[39] Cowan R D 1981 *The Theory of Atomic Structure and Spectra* (Berkeley, CA: University of California Press)

[40] Rost J M, Schulz K, Domke M and Kaindl G 1997 Resonance parameters of photo doubly excited helium *J. Phys. B: At. Mol. Opt. Phys.* **30** 4663–94

[41] Püttner R, Domke M, Grémaud B, Martins M, Schlachter A S and Kaindl G 1999 New interseries interferences in doubly-excited helium *J. Electron Spectrosc. Relat. Phenom.* **101–103** 27–32

[42] Püttner R, Grémaud B, Delande D, Domke M, Martins M, Schlachter A S and Kaindl G 2001 Statistical properties of inter-series mixing in helium: from integrability to chaos *Phys. Rev. Lett.* **86** 3747–50

[43] Schmidt V 1992 Photoionization of atoms using synchrotron radiation *Rep. Prog. Phys.* **55** 1483–659

[44] Schmidt Volker 1997 *Electron Spectrometry of Atoms using Synchrotron Radiation (Cambridge Monographs on Atomic, Molecular and Chemical Physics* no 6*)* (Cambridge: Cambridge University Press)

[45] Amusia M Ya and Chernysheva L V 1997 *Computation of Atomic Processes* (Bristol: Institute of Physics Publishing)

[46] Froese-Fischer C, Brage T and Jönsson P 1997 *Computational Atomic Structure* (Bristol: Institute of Physics Publishing)

[47] Boyle J J, Altun Z and Kelly H P 1993 Photoionization cross-section calculation of atomic tungsten *Phys. Rev.* A **47** 4811

[48] Blume M and Watson R 1962 Theory of spin–orbit coupling in atoms. I. Derivation of the spin–orbit coupling constant *Proc. R. Soc. Lond.* A **270** 127

[49] Blume M and Watson R 1963 Theory of spin–orbit coupling in atoms. II. Comparison of theory with experiment *Proc. R. Soc. Lond.* A **271** 565

[50] Slater J C 1929 The theory of complex spectra *Phys. Rev.* **34** 1293

[51] Condon E U and Shortley G H 1970 *The Theory of Atomic Spectra* (Cambridge: Cambridge University Press)

[52] Armen G B, Aksela H, Aberg T and Aksela S 2000 The resonant Auger effect *J. Phys. B: At. Mol. Opt. Phys.* **33** R49–92

[53] Snell G, Martins M, Kukk E, Cheng W T and Berrah N 2001 High resolution electron spectroscopy of a strongly correlated system: atomic barium *Phys. Rev.* A **63** 062715

[54] Nienhaus J, Zatsarinny O I and Mehlhorn W 2000 Experimental and theoretical Auger and autoionization spectra for electron impact on laser-excited Ba atoms *Phys. Essays* **13** 307–24

[55] Matila T and Aksela H 2000 Effects of electron correlation on the level width, the photoelectron, Auger electron and ion-yield spectra above the 4d threshold of Ba *J. Phys. B: At. Mol. Opt. Phys.* **33** 653–65

[56] Becker U and Shirley D A 1996 Partial cross sections and angular distributions *VUV and Soft x-ray Photoionization* (New York: Plenum) p 135

[57] Prümper G *et al* 2000 Sudden interchannel interaction in the Tl 6p ionization above the 5d threshold *Phys. Rev. Lett.* **85** 5074

[58] Rajnak K and Wybourne B G 1963 Configuration interaction effects in ℓ^N configurations *Phys. Rev.* **132** 280–90

[59] Rajnak K and Wybourne B G 1964 Electrostatically correlated spin–orbit interaction in ℓ^N-type configurations *Phys. Rev.* **134** A596–A600

[60] Bartschat K (ed) 1996 *Computational Atomic Physics* (Berlin/New York: Springer/Heidelberg)

[61] Chen M H, Crasemann B and Mark H 1981 Widths and fluorescence yields of atomic L-shell vacancy states *Phys. Rev.* A **24** 177–82

[62] Fano U 1961 Effects of configuration interaction on intensities and phase shifts *Phys. Rev.* **124** 1866

[63] Mies F H 1968 Configuration interaction theory. Effects of overlapping resonances *Phys. Rev.* **175** 164

[64] Davis L C and Feldkamp L A 1977 Interaction of many discrete states with many continua *Phys. Rev.* B **15** 2961–9

[65] Davis L C and Feldkamp L A 1978 $M_{2,3}$ spectrum of atomic Mn *Phys. Rev.* A **17** 2012–22

[66] Altun Z and Manson S T 1999 Inner-shell photoexcitation of atoms and their ions: neutral and doubly ionized Sc *J. Phys. B: At. Mol. Opt. Phys.* **32** L255–60

[67] Altun Z and Manson S T 1999 Photoionization of atomic scandium in the ground state: total cross sections and 3p → 3d resonances *Phys. Rev.* A **59** 3576–83

[68] Altun Z and Manson S T 2000 Photoelectron angular distribution of *n*s subshells of open-shell atoms as indicators of interchannel coupling: Sc 4s photoionization *Phys. Rev.* A **61** 030702

[69] Sladeczek P, Feist H, Feldt M, Martins M and Zimmermann P 1995 Photoionization experiments with an atomic beam of tungsten in the region of the 5p and 4f excitation *Phys. Rev. Lett.* **75** 1483

[70] Martins M, Sladeczek P, Tiedtke K and Zimmermann P 1998 Vacuum ultraviolet photoionization of the 5d elements in the region of the 5p and 4f excitation *Eur. Phys. J.* D **1** 47

[71] Köble U, Costello J T, Mosnier J P, Kennedy E T and Martins M 1995 XUV photoabsorption of laser generated Au vapor *J. Phys. B: At. Mol. Opt. Phys.* **28** 181–90

[72] Martins M, Sladeczek P and Zimmermann P 1996 Photoion spectra of atomic Au in the region of the 5p excitation *J. Phys. B: At. Mol. Opt. Phys.* **29** L745

[73] Martins M, Sladeczek P, Tiedtke K and Zimmermann P 1997 Photoion spectroscopy of atomic tantalum and rhenium in the region of the 5p and 4f excitation *Phys. Rev.* A **56** 1329

[74] Martins M, Sladeczek P, Tiedtke K and Zimmerman P 1997 Vacuum ultraviolet photoionization study of atomic Ir in the region of the 5p and 4f excitation *Phys. Rev.* A **55** R8

[75] Martins M 2001 Photoionisation of open-shell atoms: the chlorine 2p excitation *J. Phys. B: At. Mol. Opt. Phys.* **34** 1321–35

[76] Burke P G, Hibbert A and Robb W D 1971 Electron scattering by complex atoms *J. Phys. B: At. Mol. Phys.* **4** 153–61

[77] Seaton M J 1987 Atomic data for opacity calculations: I. General description *J. Phys. B: At. Mol. Phys.* **20** 6363–78

[78] Berrington K A, Burke P G, Butler K, Seaton M J, Storey P J, Taylor K T and Yan Y 1987 Atomic data for opacity calculations: II. Computational methods *J. Phys. B: At. Mol. Phys.* **20** 6379–97

[79] Hummer D G, Berrington K A, Eissner W, Pradhan A K, Saraph H E and Tully J A 1993 Atomic data from the IRON project. I: goals and methods *Astron. Astrophys.* **279** 298–309

[80] Nahar S N and Pradhan A K 1994 Atomic data for opacity calculations: XX. Photoionization cross sections and oscillator strengths for Fe II *J. Phys. B: At. Mol. Opt. Phys.* **27** 429–46

[81] Bautista M A 1997 Atomic data from the iron project: XX. Photoionization cross sections and oscillator strengths for Fe I *Astron. Astrophys. Suppl.* **122** 167–76

[82] Bautista M A 1999 Atomic data from the iron project: XIX. Photoionization cross sections and oscillator strengths for Ni II *Astron. Astrophys. Suppl.* **137** 529–35

[83] Donnelly D, Bell K L and Hibbert A 1998 Breit–Pauli R-matrix calculation of the 3p photoabsorption of singly ionized manganese *J. Phys. B: At. Mol. Opt. Phys.* **31** L971–6

[84] Donnelly D, Bell K L and Hibbert A 1997 Breit–Pauli R-matrix calculation of the 3p photoabsorption of singly ionized chromium *J. Phys. B: At. Mol. Opt. Phys.* **30** L285–91

[85] Donnelly D, Bell K L and Hibbert A 1996 The 3p-photoabsorption of chromium *J. Phys. B: At. Mol. Opt. Phys.* **29** L693–L697

[86] Donnelly D, Bell K L and Hibbert A 1996 3p photoabsorption of manganese II *Phys. Rev.* A **54** 974–6

[87] Berrington K A and Ballance C 2001 Double ionization yields from the photoionization of Fe II and Fe I *J. Phys. B: At. Mol. Opt. Phys.* **34** L383–90

[88] Berrington K A and Ballance C 2001 Inner-shell photoionization of the $3d^x$ ground state Fe ions *J. Phys. B: At. Mol. Opt. Phys.* **34** 2697–705

[89] Bautista M A 2000 Photoionization of Fe XV from threshold to the K-shell *J. Phys. B: At. Mol. Opt. Phys.* **33** L419–26

[90] Gorczyca T W, Pindzola M S, Robicheaux F and Badnell N R 1997 Strong interference effects in the $e^- + Sc^{3+}$ recombination cross section *Phys. Rev.* A **56** 4742–645

[91] Wöste G, Wunner G, Noble C J, Sunderland A G, Burke V M and Burke P G 2002 Electron-impact excitation of the iron peak element Fe V *J. Phys. B: At. Mol. Opt. Phys.* **35** 4847–61

[92] Sonntag B and Zimmermann P 1992 XUV spectroscopy of metal atoms *Rep. Prog. Phys.* **55** 911–87

[93] Thompson A C and Vaughan D (ed) 2001 *X-Ray Data Booklet* (Berkeley, CA: Lawrence Berkeley National Laboratory)

[94] Elder F R, Gurewitsch A M, Langmuir R V and Pollock H C 1947 Radiation from electrons in a synchrotron *Phys. Rev.* **71** 829

[95] Elder F R, Langmuir R V and Pollock H C 1948 Radiation from electrons accelerated in a synchrotron *Phys. Rev.* **74** 52

[96] Schwinger J 1949 On the classical radiation of accelerated electrons *Phys. Rev.* **75** 1912–25

[97] Madden R P and Codling K 1963 New autoionizing atomic energy levels in He, Ne, and Ar *Phys. Rev. Lett.* **10** 516–8
[98] Wille K 1991 Synchrotron radiation sources *Rep. Prog. Phys.* **54** 1005–68
[99] Ross K J and Sonntag B 1995 High temperature metal atom beam sources *Rev. Sci. Instrum.* **66** 4409–33
[100] Kennedy E T, Costello J T, Mosnier J-P and van Kamp P 2004 VUV/EUV ionising radiation and atoms and ions: dual laser plasma investigations *Rad. Phys. Chem.* **70** 291–321
[101] Lucatorto T B, McIlrath T J, Sugar J and Younger S M 1981 Radical redistribution of the 4d oscillator strength observed in the photoabsorption of the Ba, Ba^{+}, and Ba^{++} sequence *Phys. Rev. Lett.* **47** 1124–8
[102] Cooper J W, Clark C W, Cromer C L, Lucatorto T B, Sonntag B F, Kennedy E T and Costello J T 1989 Marked differences in the 3p photoabsorption between the Cr and Mn^{+} isoelectronic pair: reasons for the unique structure observed in Cr *Phys. Rev.* A **39** 6074–7
[103] Costello J T, Kennedy E T, Sonntag B F and Clark C W 1991 3p photoabsorption of free and bound Cr, Cr^{+}, Mn and Mn^{+} *Phys. Rev.* A **43** 1441
[104] Costello J T, Kennedy E T, Sonntag B F and Cromer C L 1991 XUV photoabsorption of laser-generated W and Pt vapours *J. Phys. B: At. Mol. Opt. Phys.* **24** 5063–9
[105] McGuinness C, Martins M, Wernet Ph, Sonntag B F, van Kampen P, Mosnier J-P, Kennedy E T and Costello J T 1999 Metastable state contributions to the measured 3p photoabsorption of Cr^{+} ions in a laser produced plasma *J. Phys. B: At. Mol. Opt. Phys.* **32** L583–91
[106] Costello J T, Kennedy E T, Mosnier J-P and Sayyad M H 1998 Measurement and analysis of the photoabsorption spectra of laser-produced Al and Si^{+} in the region of the 2p-subshell excitation *J. Phys. B: At. Mol. Opt. Phys.* **31** 677–88
[107] Kanngießer B *et al* 2000 Simultaneous determination of radiative and nonradiative decay channels in the neon K shell *Phys. Rev.* A **62** 014702
[108] Pahler M *et al* 1992 Angle-dependent photoelectron spectroscopy of laser-aligned atoms: Li *Phys. Rev. Lett.* **68** 2285–8
[109] Rubensson J-E, Såthe C, Cramm S, Kessler B, Stranges S, Richter R, Alagia M and Coreno M 1999 Influence of the radiative decay in the cross section for double excitations in helium *Phys. Rev. Lett.* **83** 947–50
[110] Gorczyca T W, Rubensson J-E, Sâthe C, Ström M, Agâker M, Ding D, Stranges S, Richter R and Alagia M 2000 Radiative and relativistic effects in the decay of highly excited states in helium *Phys. Rev. Lett.* **85** 1202–5
[111] Hüfner S 1995 *Photoelectron Spectroscopy (Springer Series in Solid-State Sciences* vol 82*)* (Berlin/New York: Springer/Heidelberg)
[112] Yang C N 1948 On the angular distribution in nuclear reactions and coincidence measurements *Phys. Rev.* **74** 764
[113] Cooper J W 1990 Multipole corrections to the angular distribution of photoelectrons at low energies *Phys. Rev.* A **42** 6942–5
[114] Amusia M Ya, Baltenkov A S, Chernysheva L V, Felfli Z and Msezane A Z 2001 Nondipole parameters in angular distributions of electrons in photoionization of noble-gas atoms *Phys. Rev.* A **63** 052506
[115] Grum-Grzhimailo A N 2001 Non-dipole effects in magnetic dichroism in atomic photoionization *J. Phys. B: At. Mol. Opt. Phys.* **34** L359–65
[116] Hemmers O, Whitfield S B, Glans P, Wang H, Lindle D W, Wehlitz R and Sellin I A 1998 High-resolution electron time-of-flight apparatus for the soft x-ray region *Rev. Sci. Instrum.* **69** 3809
[117] Bizau J M, Cubaynes D, Richter M, Wuilleumier F J, Obert J, Putaux J C, Morgan T J, Källne E, Sorensen S and Damany A 1991 First observation of photoelectron spectra emitted in the photoionization of a singly charged-ion beam with synchrotron radiation *Phys. Rev. Lett.* **67** 576
[118] Gottwald A, Gerth Ch and Richter M 1999 4d photoionization of free singly charged xenon ions *Phys. Rev. Lett.* **82** 2068
[119] Bizau J-M *et al* 2000 Photoionization of highly charged ions using an ECR ion source and undulator radiation *Phys. Rev. Lett.* **84** 435–8
[120] Covington A M *et al* 2001 Photoionization of metastable O^{+} ions: experiment and theory *Phys. Rev. Lett.* **87** 243002
[121] Kjeldsen H, Folkmann F, Knudsen H, Rasmussen M S, West J B and Andersen T 1999 Absolute photoionization cross section of K^{+} ions from the 3p to the 3s threshold *J. Phys. B: At. Mol. Opt. Phys.* **32** 4457–65
[122] Kjeldsen H, Kristensen B, Folkmann F and Andersen T 2002 Measurements of the absolute photoionization cross section of Fe^{+} ions from 15.8 to 180 eV *J. Phys. B: At. Mol. Opt. Phys.* **35** 3655–68
[123] West J B 2001 Photoionization of atomic ions *J. Phys. B: At. Mol. Opt. Phys.* **34** R45–R91
[124] Berrah N *et al* 2001 K-shell photodetachment of Li^{-}: experiment and theory *Phys. Rev. Lett.* **87** 253002
[125] Kjeldsen H, Andersen P, Folkmann F, Kristensen B and Andersen T 2001 Inner-shell photodetachment of Li^{-} *J. Phys. B: At. Mol. Opt. Phys.* **34** L353–7

[126] Gibson N D, Walter C W, Bozek J D, Akerman G, Martins M, McLaughlin B, Zatsirinny O, Gorczyca T and Berrah N 2003 K-shell photodetachment from C^{-1}: experiment and theory *Phys. Rev.* A **67** 030703
[127] Phaneuf R A, Havener C C, Dunn G H and Müller A 1999 Merged-beams experiments in atomic and molecular physics *Rep. Prog. Phys.* **62** 1143–80
[128] Wuilleumier F J and West J B 1996 Photoionization of excited and ionized systems *VUV and Soft X-ray Photoionization* (New York: Plenum) p 561
[129] West J B 2004 Photoionisation cross sections of atomic ions *Rad. Phys. Chem.* **70** 275–89
[130] Connerade J P, Martin M A P and Mansfield M W D 1976 Observation of a giant resonance in the 3p absorption spectrum of Mn I *Proc. R. Soc. Lond.* A **350** 405–17
[131] Mansfield M W D 1977 Excitation of the 3p-subshell in chromium vapour *Proc. R. Soc. Lond.* A **358** 253–65
[132] Bruhn R, Sonntag B and Wolff H W 1979 3p excitation of atomic and metallic Fe, Co Ni and Cu *J. Phys. B: At. Mol. Phys.* **12** 203–12
[133] Meyer M, Prescher Th, von Raven E, Richter M, Schmidt E, Sonntag B and Wetzel H-E 1986 Decay channels of core excitation resonances in 3d and 4f metal atoms *Z. Phys.* D **2** 347–62
[134] Schmidt M 1986 Einfach- und Doppelionisation an den 3d-Übergangselementen im Bereich der 3p Anregung *PhD Thesis* Technische Universität Berlin, Berlin
[135] Whitfield S B, Kehoe K, Wehlitz R, Krause M O and Caldwell C D 2001 Photoelectron spectrometry of atomic scandium in the region of the 3p → 3d giant resonance *Phys. Rev.* A **64** 022701
[136] Godehusen K, Martins M and Zimmermann P 2000 unpublished data
[137] Richter T, Godehusen K and Zimmermann P 2002 unpublished data
[138] Godehusen K, Richter T, Zimmermann P and Martins M 2003 Ion charge resolved 3p photoabsorption measurements of atomic Cr *J. Phys. B: At. Mol. Opt. Phys.* **36** L387
[139] Feist H, Feldt M, Gerth Ch, Martins M, Sladeczek P and Zimmermann P 1996 3p-photoionization resonances of atomic Fe, Co, and Ni studied by the observation of singly and doubly charged photoions *Phys. Rev.* A **53** 760
[140] Martins M 2002 On the 3p → 3d photo excitation of atomic scandium *J. Phys. B: At. Mol. Opt. Phys.* **35** L223
[141] Martins M 2005 unpublished data
[142] Verweyen A, von dem Borne A, Glatzel P, Wernet Ph, Sonntag B, Godehusen K, Gerth Ch and Zimmermann P 1999 VUV photoionization of UV-laser-tailored Ni-like Cu $3d^9$ atoms *Phys. Rev.* A **60** R737–40
[143] Dolmatov V K and Amusia M Ya 1994 Resonant structure of the 3d electrons angular distribution in a free Mn^+ ion *J. Phys. B: At. Mol. Opt. Phys.* **27** L281–5
[144] Dolmatov V K 1993 The case of a unique autoionization decay dynamic: the 3p → *n*d resonances in Cr *J. Phys. B: At. Mol. Opt. Phys.* **26** L393–8
[145] Dolmatov V K and Manson S T 1998 On the dependence of inner-shell photoionization on the outer-shell structure of Mn^+ *J. Phys. B: At. Mol. Opt. Phys.* **31** 999–1001
[146] Dolmatov V K and Manson S T 1997 'Masking' effects in the photoelectron beta-parameter spectrum *J. Phys. B: At. Mol. Opt. Phys.* **30** L517–21
[147] Connerade J P and Dolmatov V K 1997 Overlapping resonances in the β-parameter spectrum *J. Phys. B: At. Mol. Opt. Phys.* **30** L181–7
[148] Dolmatov V K 1996 Characteristic features of the 3p absorption spectra of free iron-group elements due to the duplicity of the 'inner-valence' 3d electrons. Application to Mn^{2+} *J. Phys. B: At. Mol. Opt. Phys.* **29** L687–92
[149] Connerade J P and Dolmatov V K 1996 Inner-shell 3p → 4s and 3p → 3d resonances in the photoionization of excited manganese *J. Phys. B: At. Mol. Opt. Phys.* **29** L831–5
[150] Dolmatov V K and Mansurov M M 1996 Trends in valence autoionizing Rydbergs for $n\mathrm{d}^5$ semifilled-shell ground and excited atoms and ions: Cr, Mn, Mn^+, Fe^+, Fe^{2+}, Mo, Tc, Tc^+ and Re *J. Phys. B: At. Mol. Opt. Phys.* **29** L307–12
[151] Amusia M Ya and Dolmatov V K 1993 Photoionization of inner *n*s electrons in semi-filled shell atoms (3s electrons in a Mn atom) *J. Phys. B: At. Mol. Opt. Phys.* **26** 1425–33
[152] Dolmatov V K 1993 Singularity of Cr: *n*d orbital (anti-)collapse *J. Phys. B: At. Mol. Opt. Phys.* **26** L585–8
[153] Dolmatov V K 1993 On the 3p photoabsorption cross section of free Mn^+ *J. Phys. B: At. Mol. Opt. Phys.* **26** L79–84
[154] Dolmatov V K 1992 Striking differences between the 4s photoionization of free Mn^+ and Mn^{+*} *J. Phys. B: At. Mol. Opt. Phys.* **25** L629–34
[155] Robicheaux F and Greene C H 1993 Photoionization of the scandium atom: I. General features *Phys. Rev.* A **48** 4429–40

[156] Robicheaux F and Greene C H 1993 Photoionization of the scandium atom: II. Classifications *Phys. Rev.* A **48** 4441–9
[157] Armstrong D J and Robicheaux F 1993 Photoionization of the scandium atom: III. Experimental and theoretical spectra from an excited state *Phys. Rev.* A **48** 4450–60
[158] Altun Z and Manson S T 1996 Photoionization of atomic scandium in the 3p → 3d resonance region *Europhys. Lett.* **33** 17
[159] Whitfield S B, Myers T, Bjelland M, Wehlitz R, Jimenéz-Mier J, Olalda-Velasco P and Krause M O 2002 Angular distributions of the atomic scandium 3d and 4s photoelectrons in the region of the 3p → 3d giant resonance *Phys. Rev.* A **66** 060701
[160] Schippers S *et al* 2002 Experimental link of photoionization of Sc^{2+} to photorecombination of Sc^{3+} : an application of detailed balance in a unique atomic system *Phys. Rev. Lett.* **89** 193002
[161] Schippers S *et al* 2002 Photoionization of Sc^{2+} ions by synchrotron radiation: measurements and absolute cross sections in the photon energy range 23–68 eV *Phys. Rev.* A **67** 032702
[162] Dyke J M, Gravenor B W J, Hastings M P, Josland G D and Morris A 1985 Gas phase high temperature photoelectron spectroscopy: an investigation of the transition metals scandium and vanadium *J. Electron Spectrosc. Relat. Phenom.* **35** 65–75
[163] Dohrmann Th, von dem Borne A, Verweyen A, Sonntag B, Wedowski M, Godehusen K, Zimmermann P and Dolmatov V 1996 Resonant inner-shell photoelectron spectra of ground-state and laser-excited Cr atoms *J. Phys. B: At. Mol. Opt. Phys.* **29** 4641–58
[164] West J B, Hansen J E, Kristensen B, Folkmann F and Kjeldsen H 2003 Revised interpretation of the photoionization of Cr^+ in the 3p excitation region *J. Phys. B: At. Mol. Opt. Phys.* **36** L327–33
[165] Slater J C 1974 *The Self-Consistent Field for Molecules and Solids* (New York: McGraw-Hill)
[166] Dohrmann Th and Sonntag B 1996 VUV-photoionization of laser-excited atoms *J. Electron Spectrosc. Relat. Phenom.* **79** 263–8
[167] Dolmatov V K 1996 First theoretical study of the 3p absorption cross section of free Cr^+ *J. Phys. B: At. Mol. Opt. Phys.* **29** L673–6
[168] McGuinness C, Martins M, van Kampen P, Hirsch J, Whitty W W, Mosnier J-P and Kennedy E T 2000 Vacuum-UV absorption spectrum of a laser produced chromium plasma: 3p-subshell photoabsorption by Cr^{2+} ions *J. Phys. B: At. Mol. Opt. Phys.* **33** 5077–90
[169] Whitfield S B, Wehlitz R, Krause M O and Caldwell C D 2002 Analysis of the atomic Fe 3d and 4s partial cross sections in the region of the 3p → 3d giant resonance *Surf. Rev. Lett.* **9** 1229
[170] Arp U, Federmann F, Kallne E, Sonntag B and Sorensen S L 1992 Absorption resonances in the 2p threshold of manganese atoms *J. Phys. B: At. Mol. Opt. Phys.* **25** 3747–55
[171] Arp U, Iemura K, Kutluk G, Meyer M, Nagata T, Sacchi M, Sonntag B, Yagi S and Yagishita A 1994 2p absorption spectra of atomic copper using the soft x-ray absorption and total photoion yield methods *J. Phys. B: At. Mol. Opt. Phys.* **27** 3389–98
[172] Arp U, Iemura K, Kutluk G, Nagata T, Yagi S and Yagishita A 1995 Total photoion yield of atomic chromium at the 2p threshold *J. Phys. B: At. Mol. Opt. Phys.* **28** 225–32
[173] Arp U 1993 Absorptionsspektroskopie an Atomen der Metalle Ca, Cr, Mn und Cu *PhD Thesis* Universität Hamburg, Hamburg
[174] Obst B, Richter T, Martins M and Zimmermann P 2001 Photoionisation of atomic scandium in the region of the 2p resonances *J. Phys. B: At. Mol. Opt. Phys.* **34** L657–61
[175] Godehusen K, Richter T, Martins M and Zimmermann P 2001 unpublished data
[176] Martins M, Godehusen K, Richter T and Zimmermann P 2003 2p photoionization of atomic cobalt and nickel *X-Ray and Inner-Shell Processes (AIP Conf. Proc.* vol 652*)* (New York: AIP) pp 153–8
[177] Fink J, Müller-Heinzerling Th, Scheerer B, Speier W, Hillebrecht F U, Fuggle J C, Zaanen J and Sawatzky G A 1985 2p photoabsorption of the 3d elements *Phys. Rev.* B **32** 4899–904
[178] de Groot F M F, Fuggle J C, Thole B T and Sawatzky G A 1990 2p X-ray absorption of 3d transition-metal compounds: an atomic multiplet description including the crystal field *Phys. Rev.* B **42** 5459–68
[179] de Groot F M F 1993 X-ray absorption of transition metal oxides: an overview of the theoretical approaches *J. Electron Spectrosc. Relat. Phenom.* **62** 111–30
[180] de Groot F M F and van der Laan G 1997 Collected works of Theo Thole: the spectroscopy papers *J. Electron Spectrosc. Relat. Phenom.* **1–3** 25–40
[181] de Groot F M F 2001 High resolution x-ray emission and x-ray absorption spectroscopy *Chem. Rev.* **101** 1779–808
[182] Thole B T and van der Laan G 1991 Spin polarization and magnetic dichroism in photoemission from core and valence states in localized magnetic systems *Phys. Rev.* B **44** 12424–39

[183] Thole B T and van der Laan G 1993 Sum rules for magnetic dichroism in rare earth 4f photoemission *Phys. Rev. Lett.* **70** 2499
[184] van der Laan G and Kirkman I W 1992 The 2p absorption spectra of 3d transition metal compounds in tetrahedral and octahedral symmetry *J. Phys: Condens. Matter* **4** 4189–204
[185] Richter T, Obst B, Martins M and Zimmermann P 2003 The decay of the 2p resonances of atomic scandium studied by photoelectron spectroscopy *J. Phys. B: At. Mol. Opt. Phys.* **36** 155–62
[186] van der Laan G, Surman M, Hoyland M A, Flipse C F J, Thole B T, Seino Y, Ogasawara H and Kotani A 1992 Resonant photoemission at the Ni 2p core level as a probe of electron correlation effects in nickel *Phys. Rev.* B **46** 9336–40
[187] Okada K and Kotani A 1992 Interatomic and intra-atomic configuration interactions in core-level x-ray photoemission spectra of late transition-metal compounds *J. Phys. Soc. Japan.* **61** 4619–37
[188] van der Laan G, Dhesi S S and Dudzik E 2000 On-site Coulomb interaction and exchange splitting in Ni 2p photoemission of ferromagnetic nickel *Phys. Rev.* B **61** 12277–84
[189] Zdansky E O F, Nilsson A, Tillborg H, Björneholm O, Mårtensson N, Andersen J N and Nyholm R 1993 Electronic structure of atomic adsorbates from x-ray-absorption spectroscopy: threshold effects and higher excited states *Phys. Rev.* B **48** 2632–41
[190] Malutski R, Banna M S, Braun W and Schmidt V 1985 3p photoionisation in atomic manganese: 3p down arrow angular distribution *J. Phys. B: At. Mol. Phys.* **18** 1735–42
[191] Hermsmeier B, Fadley C S, Krause M O, Jimenéz-Mier J, Gerard P and Manson S T 1988 Direct evidence from gas-phase atomic spectra for an unscreened intra-atomic origin of outer-core multiplet splittings in solid manganese compounds *Phys. Rev. Lett.* **61** 2592–5
[192] Jimenéz-Mier J, Krause M O, Gerard P, Hermsmeier B and Fadley C S 1989 Partial and total cross section and multiplet structure in the photoionization of atomic manganese *Phys. Rev.* A **40** 3712–20
[193] von dem Borne A *et al* 2000 Suppression of the low-spin multiplet components in the 3p photoelectron spectra of atomic and solid 3d metals *Phys. Rev.* A **62** 052703
[194] Gerth Ch, Tiedtke K, Martins M, Obst B, Zimmermann P, Glatzel P, Verweyen A, Wernet Ph and Sonntag B 1998 Valence satellite and 3p photoelectron spectra of atomic Fe and Cu *J. Phys. B: At. Mol. Opt. Phys.* **31** 2539–47
[195] Tiedtke K, Gerth Ch, Martins M and Zimmermann P 2001 Term-dependent lifetime broadening in the 3p photoelectron spectra of atomic Fe and Co *Phys. Rev.* A **64** 022705
[196] Tiedtke K, Gerth Ch, Kanngießer B, Obst B, Zimmermann P, Martins M and Tutay A 1999 Multiplet effects on the shape of the 3p photoelectron spectrum of atomic Ni *Phys. Rev.* A **63** 3008–12
[197] Tiedtke K, Gerth Ch, Martins M, Obst B and Zimmermann P 2000 The multiplet structure of the 3p photoelectron spectrum of atomic Sc *J. Phys. B: At. Mol. Opt. Phys.* **33** L755–60
[198] Wernet Ph, Sonntag B, Martins M, Glatzel P, Obst B and Zimmermann P 2001 Multiplet splitting and valence shell recoupling in the core-level 2p photoelectron spectrum of atomic Mn and of Mn compounds *Phys. Rev.* A **63** 050702
[199] Martins M, Godehusen K, Richter T, Wolff T and Zimmermann P 2004 2p photoelectron spectroscopy of the late 3d transition metal atoms *J. Electron Spectrosc. Relat. Phenom.* **137** 345
[200] Bagus P S, Broer R, de Jong W A, Nieuwpoort W C, Parmigiani F and Sangaletti L 2001 Reply: Bagus *et al* *Phys. Rev. Lett.* **86** 3693
[201] McGuire E 1974 Multiplet effects on the widths of photoelectron peaks *Phys. Rev.* A **10** 32–50
[202] Ogasawara H, Kotani A and Thole B T 1994 Lifetime effect on the multiplet structure of 4d x-ray-photoemission spectra in heavy rare-earth elements *Phys. Rev.* B **50** 12332–41
[203] Okada K, Kotani A, Ogasawara H, Seino Y and Thole B T 1993 Auger decay of quasiparticle states: calculation of the Ni 3p photoemission spectrum in $NiCl_2$ *Phys. Rev.* B **47** 6203–6
[204] Schmidt V 1985 Photoionization of free metal atoms using synchrotron radiation *Comment. At. Mol. Phys.* **17** 1–14
[205] Tezuka Y, Shin S, Uozumi T and Kotani A 1997 Ti 2p-, Ti 3p-, and O 1s-resonant photoemission studies of Ti_2O_3 *J. Phys. Soc. Japan* **66** 3153–8
[206] Wernet P 2000 Magnetischer Dichroismus in der Cr 2p-Photoionisation *PhD Thesis* Universität Hamburg
[207] See A K and Klebanoff L E 1995 Nature of extra-atomic core-hole screening in ferromagnetic nickel *Phys. Rev. Lett.* **74** 1454
[208] von dem Borne A 1997 Magnetischer Dichroismus in der 3p-Photoionisation Laser Polarisierter Cr-Atome *PhD Thesis* Universität Hamburg, Hamburg
[209] Hermsmeier B D, Fadley C S, Sinkovic B, Krause M O, Jimenéz-Mier J, Carlson T A, Gerard P, Manson S T and Bhattacharya S K 1993 Energy dependence of the outer core-level multiplet structures in atomic Mn and Mn-containing compounds *Phys. Rev.* B **48** 12425

[210] Bagus P S, Broer R and Ilton E S 2004 A new near degeneracy effect for photoemission in transition metals *Chem. Phys. Lett.* **394** 150
[211] Richter T, Godehusen K and Zimmermann P 2003 unpublished data
[212] Fadley C S, Shirley D A, Freeman A J, Bagus P S and Mallow J V 1969 Multiplet splitting of core-electron binding energies in transition-metal ions *Phys. Rev. Lett.* **23** 1397–401
[213] Bagus P S, Freeman A J and Sasaki F 1973 Prediction of new multiplet structure in photoemission experiments *Phys. Rev. Lett.* **30** 850–3